



**HAL**  
open science

## **Distinct metabolic programs established in the thymus control effector functions of $\gamma\delta$ T cell subsets in tumor microenvironments**

Noella Lopes, Claire McIntyre, Stefania Martin, Mathilde Raverdeau, Nital Sumaria, Ayano Kohlgruber, Gina Fiala, Leandro Agudelo, Lydia Dyck, Harry Kane, et al.

### **► To cite this version:**

Noella Lopes, Claire McIntyre, Stefania Martin, Mathilde Raverdeau, Nital Sumaria, et al.. Distinct metabolic programs established in the thymus control effector functions of  $\gamma\delta$  T cell subsets in tumor microenvironments. *Nature Immunology*, 2021, 22 (2), pp.179-192. 10.1038/s41590-020-00848-3 . hal-03121669

**HAL Id: hal-03121669**

**<https://hal.science/hal-03121669>**

Submitted on 28 Oct 2021

**HAL** is a multi-disciplinary open access archive for the deposit and dissemination of scientific research documents, whether they are published or not. The documents may come from teaching and research institutions in France or abroad, or from public or private research centers.

L'archive ouverte pluridisciplinaire **HAL**, est destinée au dépôt et à la diffusion de documents scientifiques de niveau recherche, publiés ou non, émanant des établissements d'enseignement et de recherche français ou étrangers, des laboratoires publics ou privés.

1  
2  
3  
4  
5  
6  
7  
8  
9  
10  
11  
12  
13  
14  
15  
16  
17  
18  
19  
20  
21  
22  
23  
24  
25  
26  
27  
28  
29

**Distinct metabolic programmes established in the thymus control effector functions of  $\gamma\delta$  T cell subsets in tumour microenvironments**

Noella Lopes<sup>1,8</sup>, Claire McIntyre<sup>2,8</sup>, Stefania Martin<sup>3,8</sup>, Mathilde Raverdeau<sup>4,8</sup>, Nital Sumaria<sup>3</sup>, Ayano C. Kohlgruber<sup>2</sup>, Gina J. Fiala<sup>1</sup>, Leandro Agudelo<sup>5</sup>, Lydia Dyck<sup>4</sup>, Harry Kane<sup>2,4</sup>, Aaron Douglas<sup>4</sup>, Stephen Cunningham<sup>4</sup>, Hannah Prendeville<sup>4</sup>, Roisin Loftus<sup>4</sup>, Colleen Carmody<sup>2</sup>, Philippe Pierre<sup>5,6</sup>, Manolis Kellis<sup>7</sup>, Michael Brenner<sup>2</sup>, Rafael J. Argüello<sup>5</sup>, Bruno Silva-Santos<sup>1,9</sup>, Daniel J. Pennington<sup>3,9</sup> and Lydia Lynch<sup>2,4,9</sup>

<sup>1</sup>Instituto de Medicina Molecular João Lobo Antunes, Faculdade de Medicina, Universidade de Lisboa, Lisbon, Portugal.

<sup>2</sup>Brigham and Women's Hospital, Harvard Medical School, Boston MA, USA.

<sup>3</sup>Blizard Institute, Barts and The London School of Medicine, Queen Mary University of London, London, E1 2AT, UK.

<sup>4</sup>Trinity Biomedical Science Institute, Trinity College Dublin, Dublin, Ireland.

<sup>5</sup>Aix Marseille Université, CNRS, INSERM, CIML, Centre d'Immunologie de Marseille-Luminy, Marseille, France.

<sup>6</sup>Institute for Research in Biomedicine (iBiMED) and Ildio Pinho Foundation, Department of Medical Sciences, University of Aveiro, 3810-193 Aveiro, Portugal.

<sup>7</sup>MIT Computer Science and Artificial Intelligence Laboratory, MA, USA.

<sup>8</sup> and <sup>9</sup> These authors contributed equally to this work.

Correspondence should be addressed to D.J.P. ([d.pennington@qmul.ac.uk](mailto:d.pennington@qmul.ac.uk)).

30 **Abstract**

31 Metabolic programming controls immune cell lineages and functions, but little  
32 is known about  $\gamma\delta$  T cell metabolism. Here, we found that  $\gamma\delta$  T cell subsets  
33 making either IFN- $\gamma$  or IL-17 have intrinsically distinct metabolic requirements.  
34 Whereas IFN- $\gamma^+$   $\gamma\delta$  T cells were almost exclusively dependent on glycolysis,  
35 IL-17 $^+$   $\gamma\delta$  T cells strongly engaged oxidative metabolism, with increased  
36 mitochondrial mass and activity. These distinct metabolic signatures were  
37 surprisingly imprinted early during thymic development, and were stably  
38 maintained in the periphery and within tumours. Moreover, pro-tumoural IL-  
39 17 $^+$   $\gamma\delta$  T cells selectively showed high lipid uptake and intracellular lipid  
40 storage, and were expanded in obesity, and in tumours of obese mice.  
41 Conversely, glucose supplementation enhanced the anti-tumour functions of  
42 IFN- $\gamma^+$   $\gamma\delta$  T cells and reduced tumour growth upon adoptive transfer. These  
43 findings have important implications for the differentiation of effector  $\gamma\delta$  T cells  
44 and their manipulation in cancer immunotherapy.

45

## 46 **Introduction**

47 T cells engage specific metabolic pathways to support their differentiation,  
48 proliferation and function<sup>1,2</sup>. Whereas naive  $\alpha\beta$  T cells oxidize glucose-derived  
49 pyruvate *via* oxidative phosphorylation (OXPHOS) or fatty acid oxidation  
50 (FAO) to generate ATP, most effector  $\alpha\beta$  T cells engage in aerobic glycolysis  
51 (“Warburg effect”), i.e. the conversion of glucose to lactate, to strengthen cell  
52 growth and proliferation<sup>3</sup>. On the other hand, while aerobic glycolysis is  
53 required for optimal  $\alpha\beta$  T cell effector function<sup>4,5</sup>, tumour cells heavily  
54 consume glucose in the tumour microenvironment (TME), which has a  
55 dramatic impact on cytokine production by T cells and hampers tumour  
56 immunity<sup>5,6</sup>. There is therefore great interest in understanding how  
57 metabolism-based interventions could inhibit tumour metabolism while  
58 promoting effective anti-tumour immunity for improved immunotherapeutic  
59 outcomes<sup>7</sup>.

60  $\gamma\delta$  T cells represent a promising immune population for next-generation  
61 cancer immunotherapies<sup>8,9</sup>. Since they are not MHC-restricted nor dependent  
62 on neoantigen recognition,  $\gamma\delta$  T cells constitute a complementary layer of anti-  
63 tumour immunity to their  $\alpha\beta$  T cell counterparts<sup>10</sup>. In fact, many properties of  
64  $\gamma\delta$  T cells, including sensing of “stress-inducible” changes and very rapid  
65 effector responses, align best with innate immunity, or “lymphoid stress-  
66 surveillance”<sup>11</sup>, although in some instances they display adaptive-like  
67 behaviour and profound shaping of T cell receptor (TCR) repertoires<sup>12,13</sup>.

68 The effector functions of murine  $\gamma\delta$  T cells are dominated by the production of  
69 two key cytokines, interleukin 17A (IL-17) and interferon- $\gamma$  (IFN- $\gamma$ ). Beyond  
70 contributions to immune responses against pathogens, the provision of these  
71 two cytokines by  $\gamma\delta$  T cells is important in many (patho)physiological contexts,  
72 such as maintenance of tissue homeostasis<sup>14,15</sup>, autoimmunity<sup>16</sup> and cancer<sup>8</sup>.  
73 IL-17 and IFN- $\gamma$  are mostly produced by distinct  $\gamma\delta$  T cell subsets that, unlike  
74 their CD4<sup>+</sup> T cell counterparts, typically acquire their effector functions during  
75 thymic development<sup>17,18</sup>. Thus, we and others have shown that thymic  $\gamma\delta$  T  
76 cell progenitors, driven by signals including those stemming from the TCR,

77 split into a CD27<sup>+</sup> (and CD45RB<sup>+</sup>) branch that makes IFN- $\gamma$  but not IL-17; and  
78 a CD27<sup>-</sup> (and CD44<sup>hi</sup>) pathway that selectively expresses IL-17<sup>17-21</sup>.

79 The IFN- $\gamma$ /IL-17 dichotomy between effector  $\gamma\delta$  T cell subsets is particularly  
80 relevant in cancer, since IFN- $\gamma$ -producing  $\gamma\delta$  T cells ( $\gamma\delta^{\text{IFN}}$ ) are associated with  
81 tumour surveillance and regression, whereas IL-17-secreting  $\gamma\delta$  T cells ( $\gamma\delta^{17}$ )  
82 promote primary tumour growth and metastasis, both in mice and in  
83 humans<sup>8,22</sup>. However, the molecular cues that regulate the balance between  
84 such antagonistic  $\gamma\delta$  T cell subsets in the TME remain poorly characterized.  
85 Given the strong impact of metabolic resources on anti-tumour  $\alpha\beta$  T cell  
86 responses, here we have investigated the metabolic profiles of  $\gamma\delta$  T cell  
87 subsets and how they might impact on their activities in the TME. We found  
88 that  $\gamma\delta^{\text{IFN}}$  T cells are almost exclusively glycolytic, whereas  $\gamma\delta^{17}$  T cells are  
89 strongly dependent on mitochondrial and lipid oxidative metabolism. This  
90 metabolic dichotomy is established in the thymus during  $\gamma\delta$  T cell  
91 development, and maintained in peripheral lymphoid organs and within  
92 tumours in various experimental models of cancer. We further show that the  
93 provision of glucose or lipids has major impact on the relative expansion and  
94 function of the two  $\gamma\delta$  T cell subsets, and this can be used to enhance anti-  
95 tumour  $\gamma\delta$  T cell responses.

96

97

98

99 **Results**

100 **Intra-tumoural  $\gamma\delta$  T cell subsets display distinct metabolic profiles**

101 The analysis of metabolic profiles of tumour-infiltrating  $\gamma\delta$  T cells ( $\gamma\delta$  TILs)  
102 presented a major challenge: the low numbers that can be retrieved from  
103 tumour lesions in mice are largely incompatible with techniques such as  
104 Seahorse metabolic flux analysis. To overcome this difficulty, we used a  
105 newly developed protocol, SCENITH™ (*Single Cell mEtabolism by profiling*  
106 *Translation inHibition*), which is a flow cytometry-based method for profiling  
107 energy metabolism with single cell resolution<sup>23</sup>. This method is based on  
108 metabolism-dependent translation rates and puromycin's incorporation into  
109 nascent proteins (**Supplementary Fig. 1a**). The use of specific inhibitors  
110 allows the estimation of glucose dependence, mitochondrial dependence,  
111 glycolytic capacity and fatty acid and amino acid oxidation (FaaO) capacity  
112 (**Supplementary Fig. 1b**). We employed SCENITH™ to analyze the  
113 metabolic profiles of  $\gamma\delta$  TILs isolated from tumour lesions in well-established  
114 mouse models of breast (E0771) and colon (MC38) cancer (**Fig. 1a**). In both  
115 cancer models, and at both later (**Fig. 1b,c**) and earlier time points (**Fig.**  
116 **1d,e**), we observed that  $\gamma\delta^{\text{IFN}}$  cells had substantially higher glycolytic capacity,  
117 whereas  $\gamma\delta^{17}$  cells were strongly dependent on mitochondrial activity (**Fig. 1b-**  
118 **e**). These data, obtained in cancer models, prompted us to investigate the  
119 metabolic phenotypes of  $\gamma\delta$  T cell subsets in multiple tissues at steady state.

120

121 **Peripheral  $\gamma\delta$  T cell subsets show different mitochondrial and metabolic**  
122 **phenotypes**

123 To explore the metabolic differences between  $\gamma\delta$  T cell subsets in peripheral  
124 tissues, we analysed mitochondria, given their central role in cellular  
125 metabolism. To distinguish between  $\gamma\delta^{\text{IFN}}$  and  $\gamma\delta^{17}$  cells we used CD27  
126 expression<sup>18-21</sup>. CD27<sup>-</sup>  $\gamma\delta$  ( $\gamma\delta^{17}$ ) cells displayed increased mitotracker and  
127 tetramethylrhodamine methyl ester (TMRM) staining in peripheral lymph  
128 nodes (LNs) compared to CD27<sup>+</sup>  $\gamma\delta$  ( $\gamma\delta^{\text{IFN}}$ ) cells, indicating higher  
129 mitochondrial mass (normalised to cell size) and mitochondrial membrane

130 potential ( $\Delta\Psi_m$ ), respectively (**Fig. 2a,b**). These differences were retained  
131 upon activation and expansion *in vitro* over 9-days (**Supplementary Fig. 2**).  
132 Importantly, the distinct mitochondrial phenotypes were also validated with  
133 another mitochondrial membrane potential dye, tetramethylrhodamine ethyl  
134 ester (TMRE), and were features of  $\gamma\delta^{17}$  and  $\gamma\delta^{\text{IFN}}$  cells *ex vivo* from multiple  
135 locations (**Fig. 2c**). In agreement with mitochondrial enrichment in  $\gamma\delta^{17}$  cells,  
136 seahorse metabolic flux analysis of peripheral  $\gamma\delta$  T cells showed higher levels  
137 of basal OXPHOS in  $\gamma\delta^{17}$  cells, and conversely, increased basal levels of  
138 glycolysis in  $\gamma\delta^{\text{IFN}}$  cells (**Fig. 2d-f**). These data were validated in independent  
139 experiments using SCENITH<sup>TM</sup> on splenic and LN  $\gamma\delta$  T cell subsets (**Fig. 2g**).

140 To assess if this metabolic dichotomy had an underlying transcriptional basis,  
141 we measured the mRNA levels of key mitochondrial and glycolysis-associated  
142 genes in purified peripheral  $\gamma\delta^{17}$  and  $\gamma\delta^{\text{IFN}}$  cells. We found systematic biases in  
143 gene expression that matched the differential metabolic programmes (**Fig.**  
144 **2h,i**). Of particular note is the clear-cut segregation of two master  
145 transcriptional regulators: *Nrf1*, which orchestrates mitochondrial DNA  
146 transcription<sup>24,25</sup>, found to be enriched in  $\gamma\delta^{17}$  cells (**Fig. 2h**); and *Myc*, which  
147 controls glycolysis<sup>26,27</sup>, that was highly overexpressed in  $\gamma\delta^{\text{IFN}}$  cells (**Fig. 2i**).  
148 *Myc* expression was further validated using a *Myc*-GFP reporter mouse (**Fig.**  
149 **2j**). These data collectively demonstrated that  $\gamma\delta$  T cell subsets possess  
150 distinct mitochondrial and metabolic features in peripheral organs at steady  
151 state.

152

### 153 **$\gamma\delta$ T cell subsets are metabolically programmed in the thymus**

154 We next aimed to understand when, during their differentiation, the metabolic  
155 differences between the two effector  $\gamma\delta$  T cell subsets were established. Since  
156 most  $\gamma\delta$  T cells are functionally pre-programmed in the thymus, we examined  
157  $\gamma\delta$  thymocyte sub-populations. Our recent studies have identified sequential  
158 stages of thymic  $\gamma\delta$  T cell progenitor development marked by CD24, CD44  
159 and CD45RB<sup>19</sup>. Early CD24<sup>+</sup> ( $\gamma\delta^{24+}$ ) precursors downregulate CD24 to  
160 become a CD24<sup>-</sup>CD44<sup>-</sup>CD45RB<sup>-</sup> ( $\gamma\delta^{\text{TN}}$ ) population that can generate cells

161 committed to either IL-17 or IFN- $\gamma$  expression, which display respectively  
162 CD44<sup>hi</sup>CD45RB<sup>-</sup> ( $\gamma\delta^{17}$ ) and CD44<sup>+</sup>CD45RB<sup>+</sup> ( $\gamma\delta^{\text{IFN}}$ ) phenotypes  
163 (**Supplementary Fig 3**). By using the SCENITH<sup>TM</sup> method, we found that, in  
164 both the adult (**Fig. 3a**) and newborn (**Fig. 3b**) thymus, these subsets showed  
165 the same metabolic dichotomy as in the periphery (**Fig. 2g**), although this was  
166 less distinct in  $\gamma\delta$  thymocytes, likely due to the dynamic subset segregation  
167 process<sup>19</sup>.

168 To investigate any potential switching of metabolic programming during  $\gamma\delta$   
169 thymocyte development, we first compared early thymic  $\gamma\delta$  progenitors with  
170 more mature subpopulations already committed to IL-17 or IFN- $\gamma$  production.  
171 We found that  $\gamma\delta^{24+}$  and  $\gamma\delta^{\text{TN}}$  progenitors stained highly for TMRE, that was  
172 lost when  $\Delta\Psi\text{m}$  was dissipated by the ionophore carbonyl cyanide-4-  
173 (trifluoromethoxy) phenylhydrazone (FCCP) (**Fig. 3c,d**). Interestingly,  
174 whereas  $\gamma\delta^{17}$  cells retained a high level of TMRE staining,  $\gamma\delta^{\text{IFN}}$  cells showed a  
175 marked reduction in  $\Delta\Psi\text{m}$  suggesting a metabolic switch away from OxPhos  
176 (**Fig. 3d**). Moreover, imagestream analysis of  $\gamma\delta^{17}$  cells stained with either  
177 mitotracker or TMRE revealed large and active mitochondria, in contrast with  
178  $\gamma\delta^{\text{IFN}}$  cells that displayed negligible staining for either dye (**Fig. 3e**), in line with  
179 our previous observations in peripheral subsets (**Fig. 2a-c**). Furthermore,  
180 Seahorse extracellular flux analysis showed that  $\gamma\delta^{17}$  thymocytes have both  
181 higher maximal respiration potential and spare respiratory capacity than their  
182  $\gamma\delta^{\text{IFN}}$  counterparts (**Fig. 3f,g**). Thus,  $\gamma\delta$  T cell subsets acquire distinct  
183 mitochondrial features during their acquisition of effector function in the  
184 thymus.

185 The adoption of divergent metabolic programs by thymic  $\gamma\delta$  T cell subsets  
186 suggested they could thrive under distinct metabolic environments. To begin  
187 to address this, we placed WT E15 thymic lobes in 7-day foetal thymic organ  
188 cultures (E15 + 7d FTOC) with media containing either low or high amounts of  
189 glucose (**Fig. 3h**).  $\gamma\delta^{17}$  cells were readily detected in lower glucose conditions  
190 but failed to develop to normal numbers when glucose concentrations were  
191 raised. By contrast,  $\gamma\delta^{\text{IFN}}$  cells were relatively enriched in high glucose  
192 conditions as demonstrated by a significant decrease in the  $\gamma\delta^{17}/\gamma\delta^{\text{IFN}}$  cell



193 ratio (**Fig. 3h**). We next established E15 + 7d FTOC in the presence of the  
194 glycolysis inhibitor 2-deoxy-D-glucose (2-DG), and found increased numbers  
195 of  $\gamma\delta^{17}$  cells and increased  $\gamma\delta^{17}/\gamma\delta^{\text{IFN}}$  cell ratios (**Fig. 3i**). A similar result was  
196 observed in E15 + 7d FTOC when cultured with Fasentin that blocks glucose  
197 uptake (**Supplementary Fig. 4**). By contrast, running E15 + 7d FTOC in the  
198 presence of metformin, which reduces the efficiency of OxPhos by inhibiting  
199 complex I of the electron transport chain, impaired  $\gamma\delta^{17}$  cell generation and  
200 decreased the  $\gamma\delta^{17}/\gamma\delta^{\text{IFN}}$  cell ratio (**Fig. 3j**). Collectively, these results suggest  
201 that the mitochondrial characteristics adopted by  $\gamma\delta^{17}$  and  $\gamma\delta^{\text{IFN}}$  cells during  
202 thymic development directly impact their ability to thrive in distinct metabolic  
203 environments.

204

### 205 **Distinct mitochondrial activities underlie effector fate of thymic $\gamma\delta$ T cell** 206 **precursors**

207 We next aimed to investigate the association of distinct metabolic  
208 programmes with the developmental divergence of  $\gamma\delta^{17}$  and  $\gamma\delta^{\text{IFN}}$  cells in the  
209 thymus. Although the  $\gamma\delta^{\text{TN}}$  population, i.e. the progenitor  $\gamma\delta$  cell subset that  
210 immediately precedes the surface upregulation of either CD44 or CD45RB  
211 (marking commitment to the IL-17 or IFN- $\gamma$  pathways, respectively<sup>19</sup>) was  
212 predominantly TMRE<sup>hi</sup>, we observed a fraction of cells with reduced TMRE  
213 staining that we reasoned might be transitioning to the TMRE<sup>lo</sup> state shown by  
214  $\gamma\delta^{\text{IFN}}$  cells (**Fig. 3c**). We further hypothesized that the metabolic status of  $\gamma\delta^{\text{TN}}$   
215 progenitors may predict their developmental fate. To test this, we sorted  
216 TMRE<sup>hi</sup> and TMRE<sup>lo</sup> cells from the  $\gamma\delta^{\text{TN}}$  subset obtained from E15 + 7d FTOC,  
217 and cultured them for 5-days on OP9-DL1 cells that are known to support  
218 appropriate development of thymocytes<sup>28</sup>. As predicted, virtually all cells from  
219 the TMRE<sup>lo</sup> cultures upregulated CD45RB and entered the IFN $\gamma$ -pathway  
220 (**Fig. 4a**); however, we were surprised that almost all cells from the TMRE<sup>hi</sup>  
221 cultures entered the CD44<sup>hi</sup> IL-17-pathway (**Fig. 4a**). This strongly suggests  
222 that  $\gamma\delta^{\text{TN}}$  cells have already committed to an effector fate, and that this  
223 commitment associates with distinct mitochondrial activities.

224 To pursue this hypothesis further, we tested  $\gamma\delta^{24+}$  progenitors that immediately  
225 precede the  $\gamma\delta^{\text{TN}}$  subset; again, we observed a remarkable segregation of  
226 effector fate, with the majority of  $\text{TMRE}^{\text{lo}}$   $\gamma\delta^{24+}$  cells entering the  $\text{IFN}\gamma$ -  
227 pathway, and the majority of  $\text{TMRE}^{\text{hi}}$   $\gamma\delta^{24+}$  cells entering the IL-17-pathway  
228 (**Fig. 4b**). The observation that so few  $\text{TMRE}^{\text{hi}}$   $\gamma\delta^{24+}$  cells adopt an  $\text{IFN}\gamma$ -  
229 secreting fate again suggests that most  $\gamma\delta^{24+}$  progenitors have already  
230 committed to subsequent effector function. Moreover, we found that  
231 differences in TMRE levels correlated with the known<sup>18,20,21</sup> effector biases of  
232  $V\gamma 1^+$  ( $\gamma\delta^{\text{IFN}}$ -biased) and  $V\gamma 4^+$  ( $\gamma\delta^{17}$ -biased) progenitors (**Fig. 4c**); and validated  
233 the early TMRE-based segregation of effector fates using only  $V\gamma 4^+$   
234 progenitors (**Supplementary Fig 5**). Furthermore, among  $\gamma\delta^{24+}$  thymocytes  
235 along the  $\gamma\delta^{\text{IFN}}$  pathway, we observed a progressive downregulation of TMRE  
236 levels from  $\gamma\delta^{\text{TN}}$  to  $\text{CD}44^-\text{CD}45\text{RB}^+$  cells and finally  $\gamma\delta^{\text{IFN}}$  cells (**Fig. 4d**).

237 Given that we and others<sup>20,21</sup> have previously shown a key role for TCR  
238 signalling in  $\gamma\delta^{\text{IFN}}$  thymocyte differentiation, we next asked if downregulation of  
239 TMRE levels associated with hallmarks of TCR signalling. Indeed, we found  
240 that low TMRE associated with high expression of CD73 (**Fig. 4e**), one of the  
241 best established markers of TCR signalling in  $\gamma\delta$  T cell development<sup>20,28,29</sup>.  
242 Moreover, in E15 thymic lobes, TMRE staining was reduced along with CD25  
243 downregulation, which is another hallmark of (developmentally early)  $\text{TCR}\gamma\delta$   
244 signalling<sup>18,20,21</sup> (**Fig. 4f**). Furthermore, at this E15 stage, the cells with the  
245 lowest TMRE staining were  $V\gamma 5^+$  progenitors (**Fig. 4f**) that are known to  
246 engage a Skint1-associated TCR-ligand in the thymus and to uniformly  
247 commit to the  $\text{IFN}\gamma$ -pathway<sup>30</sup>.

248 These lines of evidence suggested that  $\gamma\delta$  progenitors receiving agonist  
249  $\text{TCR}\gamma\delta$  signals shift away from OxPhos as indicated by their reduced  $\Delta\Psi\text{m}$ .  
250 To strengthen this point, we manipulated TCR signals using agonist GL3  
251 mAb, which, as expected<sup>18,19</sup>, promoted  $\gamma\delta^{\text{IFN}}$  cell development while inhibiting  
252 the  $\gamma\delta^{17}$  pathway in E17 + 6d FTOC (**Fig. 4g**). Upon specifically sorting  
253  $\text{TMRE}^{\text{hi}}$   $\gamma\delta^{24+}$  cells from E17 thymi and stimulating them with GL3 for 5h, we  
254 found a subpopulation that downregulated CD24 together with TMRE levels, in  
255 a mAb dose-dependent dose manner (**Fig. 4h**). These results strongly

256 suggest that TCR signalling leads to  $\Delta\Psi_m$  downregulation as  $\gamma\delta$  thymocytes  
257 differentiate into IFN- $\gamma$  producers.

258 To gain further molecular resolution, we performed single-cell  
259 RNAsequencing on TMRE<sup>lo</sup> and TMRE<sup>hi</sup>  $\gamma\delta^{24+}$  cells from E15 + 2d FTOC (**Fig.**  
260 **4i-l**). Using UMAP, TMRE<sup>lo</sup> cells clustered clearly away from TMRE<sup>hi</sup>  $\gamma\delta^{24+}$   
261 cells (**Fig. 4j**), and the former were enriched in genes involved in the  
262 regulation of antigen receptor signalling (**Fig. 4k**). In support of the metabolic  
263 phenotypes observed *ex vivo*, genes associated with OxPhos were enriched  
264 specifically in TMRE<sup>hi</sup>  $\gamma\delta^{24+}$  cells while genes involved in glucose metabolism  
265 were unregulated in TMRE<sup>lo</sup>  $\gamma\delta^{24+}$  cells (**Fig. 4l**).

266 These data collectively demonstrate that metabolic status of thymic  $\gamma\delta$   
267 progenitors marks their developmental fate from a very early stage.  
268 Progenitors entering the IL-17 pathway display sustained high mitochondrial  
269 activity, whereas those in the IFN- $\gamma$  pathway undergo a TCR-induced  
270 metabolic shift towards aerobic glycolysis. We next questioned how these  
271 intrinsic metabolic differences impacted the physiology of effector  $\gamma\delta$  T cell  
272 subsets.

273

#### 274 **Enrichment of lipid storage and lipid metabolism in $\gamma\delta^{17}$ cells**

275 Having shown that, in stark contrast with  $\gamma\delta^{\text{IFN}}$  cells,  $\gamma\delta^{17}$  cell generation was  
276 reduced under high glucose concentrations (**Fig. 3h**), and enhanced upon  
277 inhibition of glycolysis (**Fig. 3i**) or glucose uptake (**Supplementary Fig. 4**), we  
278 questioned whether other metabolic resources may be important for  $\gamma\delta^{17}$  cell  
279 physiology. To address this question we took advantage of reporter mice  
280 (*Zbtb16*<sup>GFP</sup>) for another marker that segregates  $\gamma\delta^{17}$  and  $\gamma\delta^{\text{IFN}}$  cells, the  
281 transcription factor PLZF (encoded by *Zbtb16*)<sup>21,14,31</sup>. We performed RNA-  
282 sequencing of lymphoid and tissue-resident  $\gamma\delta$  T cells sorted into PLZF<sup>+</sup> ( $\gamma\delta^{17}$ )  
283 and PLZF<sup>-</sup> ( $\gamma\delta^{\text{IFN}}$ ) cells (**Fig. 5a**). As expected,  $\gamma\delta^{17}$  cells across tissues  
284 expressed *Il17a*, whereas *Il17f* was also expressed in tissue-resident  $\gamma\delta^{17}$   
285 cells (**Fig. 5b**). Different metabolic pathways were associated with lymphoid  
286 versus tissue resident  $\gamma\delta$  T cells however, the genes common to  $\gamma\delta^{17}$  cells

287 across all tissues were related to lipid and mitochondrial metabolism,  
288 including glutamate transporter (*Slc1a1*), glucose/fatty acid metabolism  
289 (*Pdk4*), mitochondrial protein transport (*Ablim3*) and lipid metabolism (*Fabp1*,  
290 *Abdh5*, *Atp10a*). These data highlight genes associated with lipid metabolism  
291 as a common feature of  $\gamma\delta^{17}$  T cells across tissues. Consistent with this, LN  
292  $\gamma\delta^{17}$  cells had a higher neutral lipid content (as assessed by LipidTOX  
293 staining) than  $\gamma\delta^{\text{IFN}}$  cells (**Fig. 5 c,d**). This differential lipid content was further  
294 increased upon activation with IL-1 $\beta$ +IL-23 (**Supplementary Fig. 6a**),  
295 associated with expression of IL-17A, IL-17F and ROR $\gamma$ t (**Supplementary**  
296 **Fig. 6b**), and was observed across  $\gamma\delta$  T cells from multiple tissues, with the  
297 notable exception of the skin (**Fig. 5e**), where  $\gamma\delta$  T cells have been shown to  
298 display specific mechanisms of tissue adaptation<sup>32</sup>. In particular, V $\gamma$ 6<sup>+</sup>  $\gamma\delta$  T  
299 cells in the dermis are transcriptionally distinct from those in pLNs and display  
300 a highly activated but less proliferative phenotype. This tissue adaptation may  
301 alter the metabolic requirements of skin-resident  $\gamma\delta$  T cells. In addition,  $\gamma\delta$  T  
302 cells may adapt to utilize specific metabolites present within the skin<sup>33</sup>.

303 Imaging analysis revealed that the increased LipidTOX staining was due to  
304 the accumulation of intracellular lipid droplets in  $\gamma\delta^{17}$  cells (**Fig. 5f,g**). Lipid  
305 droplets store neutral lipids including triglycerides (TAGs) and cholesterol  
306 esters<sup>34</sup>. We found that the two  $\gamma\delta$  subsets had equivalent TAG content (**Fig.**  
307 **5h**) but free cholesterol, as determined by Filipin III staining, was higher in  
308  $\gamma\delta^{17}$  cells (**Fig. 5i**). We next questioned if  $\gamma\delta^{17}$  engaged in lipid uptake which  
309 could account for lipid storage. Using labelled palmitate (Bodipy-FL-C<sub>16</sub>), we  
310 found that  $\gamma\delta^{17}$  cells selectively took up lipids (**Fig. 5j**), which was further  
311 enhanced following activation (**Supplementary Fig. 6c**). Analysis of  $\gamma\delta$  T cell  
312 cytokine production confirmed that the ability to take up palmitate was specific  
313 to IL-17 producers (**Fig. 5l,m**). Of note, V $\gamma$ 4<sup>+</sup> and V $\gamma$ 6<sup>+</sup> (V $\gamma$ 1<sup>-</sup>V $\gamma$ 4<sup>+</sup>)  $\gamma\delta$  T cells  
314 showed a higher palmitate uptake than V $\gamma$ 1<sup>+</sup> cells (**Fig. 5n**); While V $\gamma$ 6<sup>+</sup>  $\gamma\delta$  T  
315 cells primarily produce IL-17, V $\gamma$ 4<sup>+</sup>, can produce either IFN- $\gamma$  or IL-17<sup>18,19</sup>.  
316 However, palmitate uptake was specific to V $\gamma$ 4<sup>+</sup> cells that produced IL-17 (**Fig.**  
317 **5o**). Furthermore,  $\gamma\delta^{17}$  cells also displayed higher uptake of fluorescently  
318 labelled cholesterol ester (Bodipy CholEsteryl FL-C<sub>12</sub>) (**Fig. 5k**), indicating

319 their ability to take up multiple types of lipids including fatty acids and  
320 cholesterol.

321 These data demonstrate that  $\gamma\delta^{17}$  cells have an exquisite capacity to take up  
322 and accumulate intracellular lipids, and display transcriptional signatures of  
323 enhanced lipid metabolism compared to  $\gamma\delta^{\text{IFN}}$  cells.

324

### 325 **High fat diet promotes $\gamma\delta^{17}$ cell expansion and their accumulation in** 326 **tumours**

327 We next tested the effect of a lipid-rich, high fat diet (HFD), on  $\gamma\delta$  T cell  
328 subsets *in vivo*. Unlike standard fat diet (SFD) fed mice, which alternate  
329 between using lipids or carbohydrates for fuel during light/dark cycles  
330 respectively, feeding mice a HFD reduced their respiratory exchange ratio  
331 (RER), illustrating a systemic metabolic switch to constantly burning lipids as  
332 the main fuel source. (**Fig. 6a**). We found that both the percentage and  
333 absolute number of LN  $\gamma\delta$  T cells were increased during HFD (**Fig. 6b**), which  
334 was due to a specific increase in  $\gamma\delta^{17}$  (but not  $\gamma\delta^{\text{IFN}}$ ) cells (**Fig. 6c,d**).

335 Tumours are another site reported to be lipid-rich. To explore the effect of the  
336 lipid-rich tumour environment on  $\gamma\delta^{17}$  cells, we employed the B16F10  
337 melanoma model. In SFD mice, we found an enrichment of  $\gamma\delta^{17}$  cells within  
338 the tumour compared to draining LN (dLN) or spleen (**Fig. 6e**). These  $\gamma\delta^{17}$   
339 cells were also enriched compared to  $\gamma\delta^{\text{IFN}}$  (**Fig. 6f**). Given  $\gamma\delta^{17}$  were enriched  
340 in obese mice and in the tumour, we next asked if obesity combined with the  
341 tumour model would further enhance  $\gamma\delta^{17}$  cells. Mice fed HFD exhibited  
342 enhanced tumour growth (**Fig. 6g**), and further increased percentages and  
343 numbers of tumour-infiltrating  $\gamma\delta^{17}$  cells compared to the SFD group (**Fig. 6 h-**  
344 **j**). These data demonstrate that a lipid-rich environment selectively  
345 accumulates  $\gamma\delta^{17}$  but not  $\gamma\delta^{\text{IFN}}$  cells in the tumour.

346 Given the preferential uptake of cholesterol by  $\gamma\delta^{17}$  cells (**Fig. 5i**), we next  
347 investigated its effect on  $\gamma\delta^{17}$  cell proliferation and function. We incubated  
348 purified  $\gamma\delta^{27-}$  ( $\gamma\delta^{17}$ ) cells for 5h with cholesterol-loaded cyclodextrin (CLC),  
349 which we found to promote  $\gamma\delta^{27-}$  cell proliferation when compared to control

350 culture conditions (**Fig. 6k**). To determine its impact on tumor growth *in vivo*,  
351 we injected CLC pre-treated (or control)  $\gamma\delta^{17}$  cells twice (within two days) into  
352 s.c. E0771 tumours (as established in **Fig. 1b**), which allow local T cell  
353 delivery. Strikingly,  $\gamma\delta^{17}$  cells pre-treated with CLC substantially enhanced  
354 tumour growth (**Fig. 6l-n**).

355 Conversely, we also tested the effect of reducing lipids *in vivo*, by injected  
356 orlistat, which inhibits lipases and thus prevents uptake of dietary fat, into  
357 B16F10 tumour-bearing mice. Mice injected with orlistat exhibited reduced  
358 body weight and tumour growth compared to vehicle-treated mice  
359 (**Supplementary Fig. 7a,b**). Importantly, these mice showed decreased  
360 numbers of tumour-infiltrating  $\gamma\delta^{17}$  cells, which had lower neutral lipid content  
361 (**Supplementary Fig. 7c,d**).

362 Together, these data show that lipid-rich environments promote the selective  
363 expansion of  $\gamma\delta^{17}$  cells that support tumour growth.

364

### 365 **Glucose supplementation enhances anti-tumour functions of $\gamma\delta^{\text{IFN}}$ cells**

366 We next aimed to use the knowledge gathered in this study to boost anti-  
367 tumour  $\gamma\delta$  T cell responses, which are known to rely on  $\gamma\delta^{\text{IFN}}$  cells<sup>8,22</sup>. Given  
368 our data showing that glucose promotes the development of  $\gamma\delta^{\text{IFN}}$  over  $\gamma\delta^{17}$   
369 cells in the thymus (**Fig. 3h,i**), and the higher glycolytic capacity of  $\gamma\delta^{\text{IFN}}$  cells  
370 in peripheral organs (**Fig. 2g**) and also within tumours (**Fig. 1b-e**), we  
371 hypothesized that glucose supplementation would enhance  $\gamma\delta^{\text{IFN}}$  cell  
372 functions. Further supporting this hypothesis, we found that intra-tumoural  
373  $\gamma\delta^{\text{IFN}}$  cells preferentially took up 2-NDBG when compared to  $\gamma\delta^{17}$  TILs (**Fig.**  
374 **7a**).

375 We first tested the impact of glucose on  $\gamma\delta^{17}$  and  $\gamma\delta^{\text{IFN}}$  cell functions *in vitro*.  
376 We cultured purified  $\gamma\delta^{27-}$  ( $\gamma\delta^{17}$ ) or  $\gamma\delta^{27+}$  ( $\gamma\delta^{\text{IFN}}$ ) cells in standard culture  
377 conditions containing low dose glucose (5mM) or in high glucose (50mM). We  
378 found high glucose to be detrimental to  $\gamma\delta^{17}$  cells (**Supplementary Fig. 8**), in  
379 stark contrast to  $\gamma\delta^{\text{IFN}}$  cells. Indeed, supplementation with high glucose  
380 augmented (whereas provision of 2-DG reduced) the percentage and

381 numbers of  $\gamma\delta^{\text{IFN}}$  cells (**Fig. 7b**), with parallel effects on their proliferation (**Fig.**  
382 **7c**) and on the levels of expression of both IFN- $\gamma$  (**Fig. 7d**) and its master  
383 transcriptional regulator<sup>21</sup>, T-bet (**Fig. 7e**).

384 To specifically address the importance of aerobic glycolysis for  $\gamma\delta^{\text{IFN}}$  cells, we  
385 cultured  $\gamma\delta^{\text{IFN}}$  cells with galactose (compared to glucose), since cells grown in  
386 galactose enter the pentose phosphate pathway instead of using aerobic  
387 glycolysis<sup>35,36</sup>. We observed a reduction in the percentage and absolute  
388 numbers of  $\gamma\delta^{\text{IFN}}$  cells (**Fig. 7f**), as well as in their IFN- $\gamma$  (**Fig. 7g**) and T-bet  
389 (**Fig. 7h**) expression levels, thus establishing that aerobic glycolysis is  
390 required for optimal IFN- $\gamma$  production by  $\gamma\delta^{\text{IFN}}$  cells.

391 Next we asked if the cytotoxic function of  $\gamma\delta^{\text{IFN}}$  cells was also enhanced by  
392 glucose supplementation. For this, we co-cultured  $\gamma\delta^{\text{IFN}}$  cells that were  
393 previously supplemented (or not) with high dose of glucose with E0771 breast  
394 cancer cells at different effector:target (E:T) ratios. “Glucose-enhanced”  $\gamma\delta^{\text{IFN}}$   
395 cells displayed substantially higher cytotoxic potency against the cancer cells,  
396 compared to the respective controls at each E:T ratio (**Fig. 7i**).

397 As  $\gamma\delta$  T cells are actively being pursued in the clinic as an adoptive cell  
398 therapy for cancer<sup>8</sup>, we tested whether we could use glucose supplementation  
399 to enhance the anti-tumour functions of  $\gamma\delta^{\text{IFN}}$  cells *in vivo*, in an adoptive cell  
400 transfer setting. Purified  $\gamma\delta^{\text{IFN}}$  cells were cultured in the presence or absence  
401 of high dose glucose for 5h, washed, and injected twice (within two days) into  
402 the tumour site. While control  $\gamma\delta^{\text{IFN}}$  cells produced a small yet significant  
403 reduction in tumour size, glucose substantially augmented the anti-tumour  
404 effects of  $\gamma\delta^{\text{IFN}}$  cells, essentially inhibiting tumour growth (from the time of  
405 injection) within the time window analysed (**Fig. 7j,k**). These data reveal a  
406 new, metabolism-based, means to enhance the anti-tumour functions of  $\gamma\delta$  T  
407 cells that could be explored for adoptive cell immunotherapy of cancer.

## 408 Discussion

409 Metabolism dysregulation is viewed as an immune evasion strategy in cancer.  
410 To overcome it, and thus enable anti-tumour immune responses, it is critical  
411 to understand immune cell metabolism and its interplay with tumour cells in  
412 the TME. Although our knowledge on  $\alpha\beta$  T cell metabolism has increased  
413 significantly<sup>1,3,37</sup>, little is known about  $\gamma\delta$  T cells. Here, we identified a  
414 metabolic dichotomy between the main effector  $\gamma\delta$  T cell subsets that play  
415 opposing roles in cancer immunity<sup>8,22</sup>. Whereas anti-tumoural  $\gamma\delta^{\text{IFN}}$  cells are  
416 almost exclusively glycolytic, pro-tumoural  $\gamma\delta^{17}$  cells require mitochondrial  
417 metabolism; and their activities within tumours can be promoted by glucose or  
418 lipid metabolism, respectively.

419 Unexpectedly, the metabolic dichotomy of  $\gamma\delta$  T cell subsets is established  
420 early during thymic development, which contrasts with the peripheral  
421 metabolic (re)programming of effector  $\alpha\beta$  T cells. Naïve  $\alpha\beta$  T cells require  
422 activation to undergo rewiring of cellular metabolism, namely transition from  
423 OxPhos to aerobic glycolysis, through which glucose is fermented into lactate  
424 rather than oxidized in mitochondria<sup>3</sup>. Furthermore, depending on metabolic  
425 cues in the tissue or during immune challenge, naïve T cells are pushed  
426 toward Th1, Th2, Th17 or Treg fates, dependent on intrinsic metabolic  
427 pathways engaged outside the thymus. By contrast, we show that an  
428 equivalent metabolic shift occurs in early thymic  $\gamma\delta$  progenitors as they  
429 commit to the IFN- $\gamma$  pathway, seemingly as a result of strong TCR $\gamma\delta$   
430 signalling. Indeed, analysis of various hallmarks of TCR signalling suggest  
431 that  $\gamma\delta$  progenitors receiving agonist TCR $\gamma\delta$  signals shifted away from OxPhos  
432 as indicated by their reduced  $\Delta\Psi_m$ . Moreover, upon TCR (GL3 mAb)  
433 stimulation, a small population of  $\gamma\delta$  progenitors downregulated CD24  
434 together with  $\Delta\Psi_m$  (TMRE), thus associating strong TCR $\gamma\delta$  signalling in the  
435  $\gamma\delta^{\text{IFN}}$  developmental pathway with metabolic reprogramming. This draws a  
436 parallel with  $\alpha\beta$  T cell activation, during which early TCR signalling is required  
437 for induction of aerobic glycolysis<sup>38</sup>. This acts as a switch for *Myc* mRNA (and  
438 protein) expression, such that strength of TCR stimulus determines the  
439 frequency of T cells that transcribe *Myc* mRNA<sup>36</sup>. The common denominator



440 of the metabolic switches in effector  $\gamma\delta$  and  $\alpha\beta$  T cells may thus be  
441 upregulation of Myc, which is required for transcription of genes encoding  
442 glycolytic enzymes<sup>26,27</sup>. Indeed, our data show a striking enrichment of Myc  
443 (mRNA and protein) in  $\gamma\delta^{\text{IFN}}$  cells compared to  $\gamma\delta^{17}$  cells. On the other hand,  
444 the sustained dependence of  $\gamma\delta^{17}$  cells on mitochondrial OxPhos is in line with  
445 that recently reported for their functional equivalents in the  $\alpha\beta$  T cell  
446 compartment, Th17 cells<sup>39</sup>. Of note, IL-17-producing type 3 innate lymphoid  
447 cells (ILC3) were recently shown to require both glycolysis and mitochondrial-  
448 derived ROS for activation<sup>40</sup>, but a direct comparison with type 1 ILCs is still  
449 missing.

450 The concept of TCR signalling playing a key role in the metabolic  
451 programming of  $\gamma\delta$  T cell subsets builds upon, but provides a novel  
452 perspective to, previous models of their thymic development. Thus, the  
453 unequivocal dependence on strong TCR signals for  $\gamma\delta^{\text{IFN}}$  cell  
454 differentiation<sup>20,30</sup> may be linked to a required metabolic shift to aerobic  
455 glycolysis. Moreover, the detrimental impact of agonist TCR signals on  $\gamma\delta^{17}$   
456 cell development may be due to metabolic conflict with their OxPhos  
457 requirements, documented by our FTOC experiments using specific inhibitors.  
458 Importantly, these distinct metabolic phenotypes are maintained in peripheral  
459  $\gamma\delta$  T cell subsets, which is consistent with and expands our previous  
460 epigenetic and transcriptional analyses<sup>41,42</sup>.

461 We were particularly interested to investigate the metabolic properties of  
462 peripheral  $\gamma\delta$  T cell subsets once they infiltrated tumour lesions, for which we  
463 employed three experimental models of cancer (melanoma, breast and  
464 colon). Critically, we found that the dichotomy between  $\gamma\delta^{17}$  and  $\gamma\delta^{\text{IFN}}$  subsets  
465 was preserved in the TME, which enabled metabolic interventions that may  
466 have therapeutic potential. In fact, while  $\gamma\delta$  T cell infiltration is largely  
467 perceived to associate with favourable prognosis in cancer patients<sup>43</sup>, recent  
468 clinical data have suggested that, in agreement with mouse experimental  
469 systems<sup>22</sup>, human  $\gamma\delta^{17}$  *versus*  $\gamma\delta^{\text{IFN}}$  cell subsets have antagonistic prognostic  
470 values<sup>8</sup>. Thus, improvement in the therapeutic performance of  $\gamma\delta$  T cells in the

471 clinic<sup>44</sup> is likely to require a better understanding of the factors that control the  
472 balance between  $\gamma\delta^{17}$  and  $\gamma\delta^{\text{IFN}}$  cell subsets in the TME.

473

474 Here, we also identified lipids as key  $\gamma\delta^{17}$ -promoting factors, which is  
475 particularly relevant because tumours are known to be lipid-rich  
476 microenvironments<sup>4,5,45,46</sup>. Palmitate and cholesterol ester uptake were higher  
477 in  $\gamma\delta^{17}$  than  $\gamma\delta^{\text{IFN}}$  cells, therefore we propose that increase in intracellular lipids  
478 is due to enhanced uptake, although endogenous lipid synthesis cannot be  
479 ruled out. Our findings that  $\gamma\delta^{17}$  cell proliferation is boosted by cholesterol  
480 treatment, and that these cells expand substantially in obese mice, provide  
481 additional evidence that HFD causes a systemic increase in the  $\gamma\delta^{17}$  subset,  
482 consistent with previous findings in the skin<sup>47</sup> and lungs<sup>48</sup>, and may provide a  
483 mechanistic understanding for this expansion. Obesity is a known risk factor  
484 for cancer and we previously demonstrated the link between obesity and  
485 suppression of NK cell anti-tumour function<sup>49</sup>. Given that  $\gamma\delta^{17}$  cells have  
486 strong pro-tumoural effects and we find this population to be expanded in  
487 tumours of obese mice, this may represent an additional mechanism linking  
488 cancer and obesity, whereby abundant lipids favor  $\gamma\delta^{17}$  over  $\gamma\delta^{\text{IFN}}$  cells to  
489 support tumour growth.

490 Conversely, we found  $\gamma\delta^{\text{IFN}}$  cells, from their thymic development to intra-  
491 tumoural functions, to be boosted by glucose metabolism. Naturally, the large  
492 consumption of glucose by tumour cells<sup>7</sup> creates a major metabolic constraint  
493 on  $\gamma\delta^{\text{IFN}}$  TILs. Glucose restriction can impair T cell cytokine production<sup>5,6</sup>, while  
494 production of lactate by tumour cells performing aerobic glycolysis can inhibit  
495 T cell proliferation and cytotoxic functions<sup>50</sup>. Therefore, we do not conceive  
496 glucose supplementation as an appropriate strategy to enhance endogenous  
497 T cell (including  $\gamma\delta^{\text{IFN}}$ ) responses *in vivo*. Instead, we suggest that it should be  
498 considered in protocols used to expand/differentiate  $\gamma\delta$  T cells *ex vivo* for  
499 adoptive cell therapy. Such an “*in vitro* glucose boost” may enable stronger  
500 anti-tumour activities (namely, IFN- $\gamma$  production and cytotoxicity) upon T-cell  
501 transfer, as suggested by our data using CD27<sup>+</sup>  $\gamma\delta^{\text{IFN}}$  cells in the breast cancer

502 model, although evaluation of the duration and long-term impact of this  
503 “boost” requires further investigation in slower-growing tumour models.

504 While we did not dissect the mechanistic link between aerobic glycolysis and  
505 IFN- $\gamma$  production by CD27<sup>+</sup>  $\gamma\delta^{\text{IFN}}$  cells, previous studies on  $\alpha\beta$  T cells have  
506 shown that glycolysis controls (via the enzyme GAPDH) the translation of IFN-  
507  $\gamma$  mRNA<sup>5</sup>. Moreover, glycolysis was shown to be essential for the cytotoxic  
508 activity of NK cells, namely their degranulation and Fas ligand expression,  
509 upon engagement of NK cell receptors (NKR)<sup>51</sup>. This is particularly  
510 interesting when considering the potential of a human  $\gamma\delta$  T cell product that we  
511 developed for adoptive cell therapy of cancer, Delta One T (DOT) cells<sup>9,52,53</sup>.  
512 These V $\delta$ 1<sup>+</sup> T cells are induced *in vitro* to express high levels of NKR that  
513 enhance their cytotoxicity and IFN- $\gamma$  production<sup>52-54</sup>. We therefore propose  
514 that high dose glucose should be added to the DOT protocol as to further  
515 increase their anti-tumour potential.

516 In sum, this study demonstrates that thymic differentiation of effector  $\gamma\delta$  T cell  
517 subsets, besides well-established epigenetic and transcriptional regulation,  
518 includes divergent metabolic programming that is sustained in the periphery  
519 and, in particular, in the TME. It further identifies distinct metabolic resources  
520 that control the intra-tumoural activities of  $\gamma\delta$  T cell subsets, with lipids  
521 favoring  $\gamma\delta^{17}$  cells and glucose boosting  $\gamma\delta^{\text{IFN}}$  cells, which provides a new  
522 metabolism-based angle for therapeutic intervention in cancer and possibly  
523 other diseases.

524 **Methods**

525 **Ethics statement**

526 All mouse experiments performed in this study were evaluated and approved  
527 by the institutional ethical committee (Instituto de Medicina Molecular Orbea),  
528 the national competent authority (DGAV) under the license number 019069,  
529 UK Home Office regulations and institutional guidelines under license number  
530 70/8758 and by the Institutional Animal Care and Use Committee of Brigham  
531 and Women's Hospital and Harvard Medical School, the Trinity College Dublin  
532 ethics committee. Euthanasia was performed by CO<sub>2</sub> inhalation. Anesthesia  
533 was performed by isoflurane inhalation.

534

535 **Mice and tumour cell lines**

536 C57Bl/6J WT mice and Myc-GFP mice (B6;129-Myc<sup>tm1Slek/J</sup>) were purchased  
537 from Charles River and Jackson Laboratories. PLZF-GFP (*Zbtb16*<sup>GFP</sup>) mice  
538 were generated in the laboratory of D. Sant'Angelo as described previously<sup>1</sup>.  
539 Mice were maintained under specific pathogen-free conditions. Standard food  
540 and water were given *ad libitum*. Where indicated, mice were fed high fat diet  
541 (HFD) (research diets) for 8 weeks. Mice were used at the foetal (embryonic  
542 day 14-18), neonatal (1-5 days old) or adult (6-12 weeks old) stages.

543 The E0771 murine breast adenocarcinoma cells, MC38 murine colon  
544 adenocarcinoma cells and B16.F10 melanoma cells were purchased from  
545 ATCC (Manassas, VA). Cells were maintained in Dulbecco's Modified Eagle  
546 Medium (DMEM) with 10% (vol/vol) FCS (Gibco; Thermo Fisher Scientific)  
547 and 1% (vol/vol) penicillin/streptomycin (Sigma-Aldrich).

548

549 **Tumour transplantation *in vivo***

550 Mice were injected with 1 x 10<sup>6</sup> E0771 tumour cells in fat pads, 1 x 10<sup>6</sup> MC38  
551 tumour cells or 2 x 10<sup>5</sup> cells B16 tumour cells subcutaneously into the right  
552 shaved flank. Tumour growth was measured every 2-3 days using calipers  
553 and animals were sacrificed when tumours reached a diameter (D) of 15mm,  
554 became ulcerous, or 1 or 2 weeks after tumour injection. Tumour size was

555 calculated using the following formula:  $(D1)^2 \times (D2/2)$ , D1 being the smaller  
556 value of the tumour diameter. In some experiments, mice were fed with a  
557 HFD (60% calories from lard) for 10 weeks prior to tumour injection and the  
558 HFD was continued throughout the experiment.

559

## 560 **Comprehensive Lab Animal Monitoring System**

561 Indirect calorimetry data were recorded using a Promethion Metabolic Cage  
562 System (Sable Systems) essentially as described previously<sup>2</sup>. Mice were  
563 housed individually in metabolic chambers under a 12h light/dark cycle at  
564 room temperature (22°C) with free access to food and water. Mice were  
565 acclimated for 24h in metabolic cages before recording calorimetric variables.  
566 Mice were fed either a standard chow diet or a high fat (60%) diet ad libitum  
567 for 12 weeks prior to being placed in the metabolic cages and were  
568 maintained on either diet throughout the recording.

569

## 570 **Tissue processing and cell isolation**

571 Tumours were collected and digested with 1mg/mL collagenase Type I, 0.4  
572 mg/mL collagenase Type IV (Worthington) and 10 µg/mL DNase I (Sigma-  
573 Aldrich) for 30 minutes at 37°C. Cell suspension was then filtered through a  
574 100 µm nylon cell strainer (Falcon/Corning).  $\gamma\delta$  T cells were isolated by  
575 scratching thymus, spleen and lymph node on a 70µm mesh. Lungs were  
576 minced then homogenized in RPMI 1640 using a TissueLyser (Qiagen) and  
577 filtered through 70µm mesh. Adipose tissue was processed as described  
578 previously<sup>3</sup>. Red blood cells were lysed using RBC Lysis Buffer (Biolegend) or  
579 ammonium chloride lysis buffer (made in-house). Single-cell suspensions of  
580 foetal and neonatal thymocytes were obtained by gently homogenizing thymic  
581 lobes followed by straining through 40µm strainers (BD).

582 For cell-sorting,  $\gamma\delta$  T cells were pre-enriched by depletion of CD4<sup>+</sup> and CD8<sup>+</sup> T  
583 cells, dendritic cells and B cells using biotinylated anti-CD4 (RM4-5), anti-CD8  
584 (53-6.7), anti-CD11c (N14) and anti-CD19 (6D5) antibodies with anti-biotin  
585 microbeads (Miltenyi Biotech) by QuadroMACS or  $\gamma\delta$  T cells were purified

586 using TCR $\gamma/\delta$  T Cell Isolation Kit, mouse (Miltenyi Biotec). Cells were sorted  
587 on a FACS Aria (BD Biosciences).

588

## 589 **Cell Culture**

590 CD27<sup>-</sup>  $\gamma\delta$  T cells were expanded *in vitro* as previously described<sup>4</sup>. This  
591 protocol was adapted to expand CD27<sup>+</sup>  $\gamma\delta$  T cells by using 10ng/ml IL-2,  
592 10ng/ml IL-15 and 20ng/ml IL-7. For downstream assays,  $\gamma\delta$  T cells were  
593 purified using TCR $\gamma/\delta$  T Cell Isolation Kit, mouse (Miltenyi Biotec). *Ex vivo*  
594 cultures were performed using RPMI 1640 (Gibco) supplemented with 10%  
595 heat-inactivated foetal bovine serum (Gibco), 1% penicillin/streptomycin, 1%  
596 L-glutamine. For cytokine stimulation, cells were cultured with 10ng/ml IL-1 $\beta$   
597 and IL-23 (Miltenyi Biotec) and/or IL-12 and IL-18 (BioLegend).

598 For short-term skin-draining-lymphocyte cultures, single-cell suspensions of  
599 lymphocytes were isolated from skin-draining lymph nodes from adult B6  
600 mice. Cells were resuspended in complete RPMI medium (RPMI-1640 with  
601 10% FCS, 1% penicillin and streptomycin, and 2 mM L-glutamine).  $1 \times 10^6$   
602 lymphocytes in 500  $\mu$ l of complete medium were incubated for 48h in 48-well  
603 plates either under control conditions or with the addition of 5-aminoimidazole-  
604 4-carboxamide (AICAR; 1.6 mM; Sigma-Aldrich). Cells were subsequently  
605 analysed by flow cytometry.

606

## 607 **Foetal Thymic Organ Cultures (FTOC)**

608 E15-E17 thymic lobes from B6 mice were cultured on nucleopore membrane  
609 filter discs (Whatman) in FTOC medium (RPMI-1640 with 10% FCS, 1%  
610 penicillin and streptomycin, 50  $\mu$ M  $\beta$ -mercaptoethanol (Invitrogen), and 2 mM  
611 L-glutamine (Sigma-Aldrich)) for 6-12 days (unless otherwise indicated). In  
612 some experiments 2-deoxyglucose (2-DG; 0.6 mM), fasentin (0.6 mM),  
613 metformin (2 mM) or oligomycin (1 nM) were added to the cultures. All thymic  
614 organ cultures were subsequently analysed by flow cytometry. In some  
615 cultures, where concentration of glucose was manipulated, "basic" FTOC

616 medium (RPMI-1640 [-] glucose with 10% FCS, 1% penicillin and  
617 streptomycin, 50  $\mu$ M  $\beta$ -mercaptoethanol (Invitrogen), and 2 mM L-glutamine  
618 (Sigma-Aldrich)) was used, and glucose was added at 5mM for “low-glucose”  
619 conditions or 25mM for “high-glucose” conditions.

620 In some experiments, anti-TCR $\delta$  antibody (GL3; 1 $\mu$ g/ml unless otherwise  
621 indicated) was added to the cultures. Cultures containing antibody were  
622 rested overnight in fresh FTOC medium before analysis. All thymic organ  
623 cultures were subsequently analysed by flow cytometry.

624

### 625 **Manipulation of $\gamma\delta$ metabolic pathways *in vitro* and *in vivo***

626 Spleen and lymph nodes were harvested from C57Bl/6J mice. Cell  
627 suspensions were stained with LIVE/DEAD Fixable Near-IR (Thermo Fisher  
628 Scientific), anti-CD3 $\epsilon$  (145-2C11), anti-TCR $\delta$  (GL3), and anti-CD27 (LG.7F9)  
629 for 15 minutes at 4°C. CD27<sup>+</sup> and CD27<sup>-</sup>  $\gamma\delta$  T cells were FACS-sorted. CD27<sup>+</sup>  
630 and CD27<sup>-</sup>  $\gamma\delta$  T cells were incubated on plate-bound anti-CD3 $\epsilon$  (145.2C11)  
631 (10  $\mu$ g/mL) in the presence of IL-7 (50  $\mu$ g/mL) or IL-7 (50  $\mu$ g/mL), IL-1 $\beta$  (10  
632  $\mu$ g/mL) and IL-23 (10  $\mu$ g/mL), respectively. All cytokines were purchased from  
633 Peprotech. Then, cells were cultured with 2-Deoxy-D-Glucose (2-DG; 2mM;  
634 Sigma-Aldrich), high D-glucose (50mM; Sigma-Aldrich), galactose (20mM;  
635 Sigma-Aldrich), Carbonyl cyanide 4-(trifluoromethoxy) phenylhydrazone  
636 (FCCP; 1 $\mu$ M; Sigma-Aldrich) and cholesterol-loaded cyclodextrin (CLC;  
637 5  $\mu$ g/mL) for 5h at 37°C for *in vitro* experiments.

638 For experiments *in vivo*, purified CD27<sup>-</sup> and CD27<sup>+</sup>  $\gamma\delta$  T cells were incubated  
639 (or not) for 5h with cholesterol-loaded cyclodextrin (5  $\mu$ g/mL) or with high D-  
640 glucose (50mM; Sigma-Aldrich), respectively. 5 x 10<sup>5</sup> CD27<sup>-</sup> or 1 x 10<sup>6</sup> CD27<sup>+</sup>  
641  $\gamma\delta$  T cells were injected twice directly at the tumor site (1<sup>st</sup> injection 7 days  
642 after tumour inoculation and 2<sup>nd</sup> injection 2 days later). Mice were analyzed 11  
643 days after tumour cell injection.

644 For lipid depletion *in vivo*, mice were injected daily with 50mg/kg Orlistat i.p.  
645 on days 6-9 after tumour injection, then tumour cell infiltrate was analysed on  
646 day 10.

647 **Killing assays for CD27<sup>+</sup>  $\gamma\delta$  T cells *in vitro***

648 Purified CD27<sup>+</sup>  $\gamma\delta$  T cells were supplemented (or not) with high levels of  
649 glucose (50mM; Sigma-Aldrich) for 5h at 37°C, 5% CO<sub>2</sub>. Then, variable  
650 numbers of CD27<sup>+</sup>  $\gamma\delta$  T cells were co-cultured with 5 x 10<sup>5</sup> E0771 breast  
651 cancer cells in complete RPMI Medium (minus D-Glucose). The killing  
652 capacities of CD27<sup>+</sup>  $\gamma\delta$  T cells based on death of E0771 cells (Annexin V  
653 staining) was assessed by flow cytometry after 24h.

654

655 **Flow cytometry**

656  $\gamma\delta$  T cells were analysed by flow cytometry using standard procedures. For  
657 surface staining, cells were Fc-blocked with anti-CD16/32 (clone 93;  
658 eBioscience) and incubated for 15 minutes at 4°C with antibodies and  
659 LIVE/DEAD Fixable Near-IR (Thermo Fisher Scientific) or viability dye Zombie  
660 NIR stain (BioLegend) in FACs buffer (PBS 1X, 10% FCS, 0.5M EDTA). Anti-  
661 CD3 $\epsilon$  (145-2C11), anti-CD27 (LG.7F9), anti-CD25 (PC61), anti-CD73  
662 (TY/11.8) and anti-V $\gamma$ 2 (UC3-10A6) were purchased from eBioscience. Anti-  
663 CD45 (30-F11), anti-TCR $\delta$  (GL3), anti-CD24 (M1/69), anti-V $\gamma$ 1 (2.11), anti-V $\gamma$ 4  
664 (UC3-10A6), anti-V $\gamma$ 5 (536) and anti-CD45RB (C363-16A) were purchased  
665 from BioLegend and anti-CD44 (IM7) from BD Pharmingen. Cells were  
666 washed with FACS buffer. For intracellular cytokine staining, cells were  
667 stimulated with 50  $\mu$ g/mL phorbol 12-myristate 13-acetate (PMA; Sigma-  
668 Aldrich) and 1  $\mu$ g/mL ionomycin (Sigma-Aldrich) for 3-4 hours at 37°C, 5%  
669 CO<sub>2</sub> in the presence of 10  $\mu$ g/mL brefeldin-A (Sigma-Aldrich) and 2  $\mu$ M  
670 monensin (eBioscience). Cells were fixed and permeabilized with Foxp3  
671 staining kit (eBioscience/Thermo Fisher Scientific), according to the  
672 manufacturer's instructions. Cells were incubated for 30 minutes at 4°C, with  
673 the following antibodies from eBioscience: anti-IFN- $\gamma$  (XMG1.2), anti-IL-17  
674 (TC11-18H10.1), Ki67 (16A8), T-bet (4B10) and ROR $\gamma$ t (B2D). For Annexin V  
675 staining, Annexin V Kit (eBioscience) was used following manufacturer's  
676 instructions.



677 The following dyes were purchased from Invitrogen and stained according to  
678 manufacturer's instructions: Mitotracker™ Green FM, Tetramethylrhodamine  
679 Methyl Ester Perchlorate (TMRM), HCS LipidTOX™ Red Neutral Lipid Stain.  
680 Palmitate uptake was measured using 1μM Bodipy FL-C<sub>16</sub> (Invitrogen)  
681 incubated for 10mins at 37°C. Cholesterol ester uptake was measured using  
682 2μM Bodipy CholEsteryl FL-C<sub>12</sub> incubated for 1h at 37°C. Cholesterol content  
683 was measured using 50μg/ml Filipin III (Sigma-Aldrich) incubated for 1h at  
684 room temperature.

685 Flow cytometry analysis was performed with a FACS Fortessa, LSRII or  
686 Canto II (BD Biosciences) and data analysed using FlowJo software (BD  
687 Biosciences).

688

#### 689 **Metabolism profile of cells**

690 Seahorse Metabolic Flux Analysis: Real-time analysis of oxygen consumption  
691 rates (OCR) and extracellular-acidification rates (ECAR) of IFN-γ- and IL-17-  
692 committed γδ T cells sorted from 5-day-old B6 pups and CD27<sup>+/-</sup> γδ T cells  
693 from spleen/lymph nodes expanded *in vitro* were assessed using the XFp  
694 Extracellular Flux or Seahorse XFe-96 analyzers, respectively (Seahorse  
695 Bioscience). Cells were added to a Seahorse XF96 Cell Culture Microplate  
696 (Agilent), coated with Cell-Tak (Corning) to ensure adherence, and sequential  
697 measurements of ECAR and OCR were performed in XF RPMI Seahorse  
698 medium supplemented with glucose (10mM), glutamine (2mM), and sodium  
699 pyruvate (1mM) following the addition of Oligomycin A (2μM), FCCP (2μM),  
700 rotenone (1μM) plus antimycin A (1-4μM). Basal glycolysis, glycolytic  
701 capacity, basal mitochondrial respiration and maximal mitochondrial  
702 respiration were calculated. OCR and ECAR values were normalized to cell  
703 number.

704

#### 705 **SCENITH™**

706 Cells were plated at 20 × 10<sup>6</sup> cells/ml in 96-well plates. After activation of γδ T  
707 cells, cells were treated for 30 minutes at 37°C, 5% CO<sub>2</sub> with Control (Co), 2-

708 Deoxy-D-Glucose (DG; 100mM; Sigma-Aldrich), Oligomycin (O; 1 $\mu$ M; Sigma-  
709 Aldrich) or a combination of both drugs (DGO). Puromycin (Puro, 10 $\mu$ g/ml;  
710 Sigma-Aldrich) is added during 15 minutes at 37°C. SCENITH™ kit  
711 (<http://www.scenith.com>) containing all reagents and protocols were kindly  
712 provided by Dr. Rafael Argüello, (CIML). Cells were washed in cold PBS and  
713 stained with primary conjugated antibodies against different surface markers  
714 (as described above) for 15 minutes at 4°C in FACS buffer (PBS 1X 5% FCS,  
715 2mM EDTA). After washing with FACS buffer, cells were fixed and  
716 permeabilized using Cytotfix/Cytoperm™ (BD) following manufacturer's  
717 instructions. Intracellular staining of puromycin using the anti-Puro monoclonal  
718 antibody (1:600, Clone R4743L-E8) was performed by incubating cells during  
719 30min at 4°C diluted in Permwash. Experimental duplicates were performed in  
720 all conditions.

721

#### 722 ***In vivo* glucose uptake**

723 2-NBDG (300 $\mu$ g diluted in PBS 1X; Cayman chemical) was injected i.v. in  
724 C57Bl/6J mice; 15min later, cells from tumours were harvested.

725

#### 726 **Assessment of mitochondrial morphology**

727 Mitochondrial membrane potential was measured using  
728 tetramethylrhodamine, ethyl ester (TMRE; 100nM; Abcam) according to  
729 manufacturer protocols. Following TMRE staining, carbonyl cyanide-4-  
730 (trifluoromethoxy) phenylhydrazone (FCCP; 25 $\mu$ M; Abcam) was used as a  
731 positive control for mitochondrial membrane depolarization. Total  
732 mitochondrial mass was assessed using MitoTracker Green (Invitrogen)  
733 according to manufacturer's instructions. All cells were subsequently analysed  
734 by flow cytometry.

735

#### 736 **Triglyceride Quantification**

737 Triglycerides (TAGs) were quantified from expanded  $\gamma\delta$  T cells *in vitro* using  
738 Picoprobe Triglyceride Quantification Assay Kit, Fluorometric (Abcam) and  
739 absorbance measured using FLUOstar OPTIMA (BMG Labtech).

740

741

#### 742 **RNA isolation and real-time PCR**

743 mRNA was prepared from FACS-sorted CD27<sup>+</sup> and CD27<sup>-</sup>  $\gamma\delta$  T cells from WT  
744 spleen and draining lymph nodes using High Pure RNA Isolation kit (Roche).  
745 Reverse transcription was performed with random oligonucleotides  
746 (Invitrogen). Results were normalized to actin mRNA. qPCR was performed  
747 with SYBR Premix Ex Taq master mix (Takara) on an ABI ViiA7 cycler  
748 (Applied Biosystems). The CT for the target gene was subtracted from the CT  
749 for the endogenous reference, and the relative amount was calculated as  
750  $2^{-\Delta\text{CT}}$ .

751

#### 752 **Imaging**

753 Thymocytes from B6 E15 thymic lobes cultured for 12 days were isolated and  
754 stained for surface markers and then Mitotracker Green or TMRE (as  
755 described above). All cells were subsequently analysed on an ImageStream<sup>™</sup>  
756 Mark II imaging flow cytometer (Amnis); 30k events were saved from samples  
757 and 1k positive events from compensation single color controls. Analysis was  
758 performed using IDEAS® version 6.2.

759 For lipid droplet quantification, expanded  $\gamma\delta$  T cells *in vitro* were stained with  
760 LipidTOX red neutral lipid stain (Invitrogen) and Hoechst 33342 (Sigma-  
761 Aldrich). Mitotracker Green FM (Invitrogen) was used to identify mitochondria.  
762 Cells were mounted onto poly-L-lysine coated slides. Images were obtained  
763 with a Zeiss LSM 800 confocal microscope using Zen 2.3 software (Zeiss)  
764 and analyzed using ImageJ.

765

#### 766 **RNA-sequencing and data processing**

767 Single-cell sequencing libraries were generated using the Chromium™ Single  
768 Cell 5' Library and Gel Bead Kit (10X Genomics) according to the  
769 manufacturer's instructions. Data was analysed using the R package Seurat  
770 v2.3<sup>5,6</sup>.

771 UMI counts were normalized using regularized negative binomial regression  
772 with the SCTransform package<sup>7</sup>. For downstream analysis of normalized data  
773 principal component analysis (PCA) was performed using n=50 dimensions  
774 and PCA variability was determined using an Elbow plot. Differential gene  
775 expression analysis and GSEA was performed using the MAST and fgsea  
776 packages<sup>6,7</sup>. Pathways and gene lists for gene set enrichment analysis were  
777 obtained using the misgdbR package from Molecular Signatures database  
778 (MSigDB)<sup>8,9</sup>. Adaptively-thresholded Low Rank Approximation (ALRA) from  
779 the Seurat wrappers package was performed to correct for drop-out values for  
780 visualization of leading-edge and differentially expressed genes identified by  
781 MAST<sup>10</sup>. The accession codes for single-cell RNA sequencing  
782 are GSE150585 and GSE156782.

783 All downstream analysis was performed using R v.3.6.3 and RStudio Desktop  
784 1.2.5001 on an Ubuntu 19.10 linux (64 bit) system using the following R  
785 packages and libraries: dplyr v.0.8.5, fgsea v.1.12.0, ggplot2 v.3.3.0, MAST  
786 v.1.12.0, SCTransform v.0.2.1, Seurat v.3.1.4, SeuratWrappers v.0.1.0, uwot  
787 v.0.1.8 and viridis v.0.5.1.

788

## 789 **Statistical analysis**

790 Statistical analysis was performed using GraphPad Prism software using non-  
791 parametric two-tailed Mann-Whitney test or, if both groups followed a normal  
792 distribution (tested by D'Agostino and Pearson normality test), using two-  
793 tailed unpaired Student *t* test or one-way analysis of variance. All data are  
794 presented as means ± standard error of mean (SEM) or standard deviation  
795 (SD). \**p* < 0.05; \*\**p* < 0.01; \*\*\**p* < 0.001, \*\*\*\*<0.0001.

796

797 1. Lynch, L. *et al.* Regulatory iNKT cells lack expression of the transcription  
798 factor PLZF and control the homeostasis of T reg cells and macrophages in

- 799 adipose tissue. *Nat. Immunol.* **16**, 85–95 (2015).
- 800 2. Vu, J. P. *et al.* Long-Term Intake of a High-Protein Diet Affects Body  
801 Phenotype, Metabolism, and Plasma Hormones in Mice. *J. Nutr.* **147**, 2243–  
802 2251 (2017).
- 803 3. Kohlgruber, A. C. *et al.*  $\gamma\delta$  T cells producing interleukin-17A regulate adipose  
804 regulatory T cell homeostasis and thermogenesis. *Nat. Immunol.* **19**, (2018).
- 805 4. McKenzie, D. R. *et al.* IL-17-producing  $\gamma\delta$  T cells switch migratory patterns  
806 between resting and activated states. *Nat. Commun.* **8**, 15632 (2017).
- 807 5. Butler, A., Hoffman, P., Smibert, P., Papalexi, E. & Satija, R. Integrating  
808 single-cell transcriptomic data across different conditions, technologies, and  
809 species. *Nat. Biotechnol.* **36**, 411–420 (2018).
- 810 6. Stuart, T. *et al.* Comprehensive Integration of Single-Cell Data Resource  
811 Comprehensive Integration of Single-Cell Data. *Cell* **177**, (2019).
- 812 7. Hafemeister, C. & Satija, R. Normalization and variance stabilization of single-  
813 cell RNA-seq data using regularized negative binomial regression. *Genome*  
814 *Biol.* **20**, 296 (2019).
- 815 8. Subramanian, A. *et al.* Gene set enrichment analysis: A knowledge-based  
816 approach for interpreting genome-wide expression profiles. *Proc. Natl. Acad.*  
817 *Sci. U. S. A.* **102**, 15545–15550 (2005).
- 818 9. Liberzon, A. *et al.* Databases and ontologies Molecular signatures database  
819 (MSigDB) 3.0. *Bioinforma. Appl. NOTE* **27**, 1739–1740 (2011).
- 820 10. Linderman, G. C., Zhao, J. & Kluger, Y. Zero-preserving imputation of scRNA-  
821 seq data using low-rank approximation. *bioRxiv* 397588 (2018).  
822 doi:10.1101/397588
- 823
- 824
- 825

826 **Acknowledgments**

827 We are grateful for the valuable assistance of the staff of the flow cytometry,  
828 bioimaging and animal facilities at our Institutions. We thank Ana Magalhães,  
829 Julie Ribot, Karine Serre, and Natacha Sousa (iMM) for technical suggestions  
830 and administrative help. This work was supported by the European Research  
831 Council (CoG\_646701 to B.S.-S.; Stg\_679173 to L.L.), Wellcome Trust  
832 (092973/Z/10/Z to D.J.P.), Science Foundation Ireland (SFI) (16/FRL/3865 to  
833 L.L), NIH (NS115064, HG008155, AG062377 to M.K), R01 AI134861,  
834 Biotechnology and Biological Sciences Research Council (BBSRC) UK  
835 (BB/R017808/1 to D.J.P) and Astrazeneca (Prémio FAZ Ciência 2019 to B.S.-  
836 S. and N.L.). N.L is supported by a post-doctoral fellowship from EMBO  
837 (ALTF 752-2018); S.M. was supported by a studentship from Medical  
838 Research Council (MRC) UK; G.F. is supported by a European Commission  
839 Marie Skłodowska-Curie Individual Fellowship (ref. 752932); and A.D, S.C.  
840 L.D and H.P are supported by Irish Research Council fellowships.

841

842 **Author contributions**

843 N.L, C.M, S.M and M.R performed most of the experiments and analyzed the  
844 data. G.F. designed and performed some experiments. N.S., A.K., L.D., H.K.,  
845 A.D., S.C., H.P. R.L. and C.C. provided technical assistance in some  
846 experiments. M.K. and L.A performed bioinformatic analysis and M.B provided  
847 reagents, materials and support. R.A. provided key assistance with the  
848 SCENITH™ methodology. B.S.-S., D.P and L.L conceived and supervised the  
849 study. N.L, C.M., B.S.-S., D.J.P. and L.L. wrote the manuscript.

850

851

852

853 **References**

- 854 1 Buck, M. D., Sowell, R. T., Kaech, S. M. & Pearce, E. L. Metabolic  
855 Instruction of Immunity. *Cell* **169**, 570-586,  
856 doi:10.1016/j.cell.2017.04.004 (2017).
- 857 2 Almeida, L., Lochner, M., Berod, L. & Sparwasser, T. Metabolic  
858 pathways in T cell activation and lineage differentiation. *Semin*  
859 *Immunol* **28**, 514-524, doi:10.1016/j.smim.2016.10.009 (2016).
- 860 3 Geltink, R. I. K., Kyle, R. L. & Pearce, E. L. Unraveling the Complex  
861 Interplay Between T Cell Metabolism and Function. *Annu Rev Immunol*  
862 **36**, 461-488, doi:10.1146/annurev-immunol-042617-053019 (2018).
- 863 4 Cham, C. M., Driessens, G., O'Keefe, J. P. & Gajewski, T. F. Glucose  
864 deprivation inhibits multiple key gene expression events and effector  
865 functions in CD8+ T cells. *Eur J Immunol* **38**, 2438-2450,  
866 doi:10.1002/eji.200838289 (2008).
- 867 5 Chang, C. H. *et al.* Posttranscriptional control of T cell effector function  
868 by aerobic glycolysis. *Cell* **153**, 1239-1251,  
869 doi:10.1016/j.cell.2013.05.016 (2013).
- 870 6 Chang, C. H. *et al.* Metabolic Competition in the Tumor  
871 Microenvironment Is a Driver of Cancer Progression. *Cell* **162**, 1229-  
872 1241, doi:10.1016/j.cell.2015.08.016 (2015).
- 873 7 O'Sullivan, D., Sanin, D. E., Pearce, E. J. & Pearce, E. L. Metabolic  
874 interventions in the immune response to cancer. *Nat Rev Immunol* **19**,  
875 324-335, doi:10.1038/s41577-019-0140-9 (2019).
- 876 8 Silva-Santos, B., Mensurado, S. & Coffelt, S. B. gammadelta T cells:  
877 pleiotropic immune effectors with therapeutic potential in cancer. *Nat*  
878 *Rev Cancer* **19**, 392-404, doi:10.1038/s41568-019-0153-5 (2019).
- 879 9 Sebestyen, Z., Prinz, I., Dechanet-Merville, J., Silva-Santos, B. &  
880 Kuball, J. Translating gammadelta (gammadelta) T cells and their  
881 receptors into cancer cell therapies. *Nat Rev Drug Discov* **19**, 169-184,  
882 doi:10.1038/s41573-019-0038-z (2020).

- 883 10 Chien, Y. H., Meyer, C. & Bonneville, M. gammadelta T cells: first line  
884 of defense and beyond. *Annu Rev Immunol* **32**, 121-155,  
885 doi:10.1146/annurev-immunol-032713-120216 (2014).
- 886 11 Hayday, A. C. Gammadelta T cells and the lymphoid stress-  
887 surveillance response. *Immunity* **31**, 184-196,  
888 doi:10.1016/j.immuni.2009.08.006 (2009).
- 889 12 Hayday, A. C. gammadelta T Cell Update: Adaptate Orchestrators of  
890 Immune Surveillance. *J Immunol* **203**, 311-320,  
891 doi:10.4049/jimmunol.1800934 (2019).
- 892 13 Ravens, S. *et al.* Human gammadelta T cells are quickly reconstituted  
893 after stem-cell transplantation and show adaptive clonal expansion in  
894 response to viral infection. *Nat Immunol* **18**, 393-401,  
895 doi:10.1038/ni.3686 (2017).
- 896 14 Kohlgruber, A. C. *et al.* gammadelta T cells producing interleukin-17A  
897 regulate adipose regulatory T cell homeostasis and thermogenesis. *Nat*  
898 *Immunol* **19**, 464-474, doi:10.1038/s41590-018-0094-2 (2018).
- 899 15 Ribeiro, M. *et al.* Meningeal gammadelta T cell-derived IL-17 controls  
900 synaptic plasticity and short-term memory. *Sci Immunol* **4**,  
901 doi:10.1126/sciimmunol.aay5199 (2019).
- 902 16 Papotto, P. H., Ribot, J. C. & Silva-Santos, B. IL-17(+) gammadelta T  
903 cells as kick-starters of inflammation. *Nat Immunol* **18**, 604-611,  
904 doi:10.1038/ni.3726 (2017).
- 905 17 Jensen, K. D. *et al.* Thymic selection determines gammadelta T cell  
906 effector fate: antigen-naive cells make interleukin-17 and antigen-  
907 experienced cells make interferon gamma. *Immunity* **29**, 90-100,  
908 doi:10.1016/j.immuni.2008.04.022 (2008).
- 909 18 Ribot, J. C. *et al.* CD27 is a thymic determinant of the balance between  
910 interferon-gamma- and interleukin 17-producing gammadelta T cell  
911 subsets. *Nat Immunol* **10**, 427-436, doi:10.1038/ni.1717 (2009).
- 912 19 Sumaria, N., Grandjean, C. L., Silva-Santos, B. & Pennington, D. J.  
913 Strong TCRgammadelta Signaling Prohibits Thymic Development of IL-



- 914 17A-Secreting gammadelta T Cells. *Cell Rep* **19**, 2469-2476,  
915 doi:10.1016/j.celrep.2017.05.071 (2017).
- 916 20 Munoz-Ruiz, M. *et al.* TCR signal strength controls thymic  
917 differentiation of discrete proinflammatory gammadelta T cell subsets.  
918 *Nat Immunol* **17**, 721-727, doi:10.1038/ni.3424 (2016).
- 919 21 Munoz-Ruiz, M., Sumaria, N., Pennington, D. J. & Silva-Santos, B.  
920 Thymic Determinants of gammadelta T Cell Differentiation. *Trends*  
921 *Immunol* **38**, 336-344, doi:10.1016/j.it.2017.01.007 (2017).
- 922 22 Silva-Santos, B., Serre, K. & Norell, H. gammadelta T cells in cancer.  
923 *Nat Rev Immunol* **15**, 683-691, doi:10.1038/nri3904 (2015).
- 924 23 Argüello, R., Combes AJ., Char, R., Gigan, JP., Baaziz, Al., Bousiquot,  
925 E., Camosseto, V., Samad, B., Tsui, J., Yan, P., Boissoneau, S.,  
926 Figarella-Branger, D., Gatti, E., Tabouret, E., Krummel, MF and Pierre,  
927 P. SCENITH: A flow cytometry based method for functional profiling  
928 energy metabolism with single cell resolution. *Cell Metabolism (in*  
929 *Press)* (2020).
- 930 24 Gleyzer, N., Vercauteren, K. & Scarpulla, R. C. Control of mitochondrial  
931 transcription specificity factors (TFB1M and TFB2M) by nuclear  
932 respiratory factors (NRF-1 and NRF-2) and PGC-1 family coactivators.  
933 *Mol Cell Biol* **25**, 1354-1366, doi:10.1128/MCB.25.4.1354-1366.2005  
934 (2005).
- 935 25 Scarpulla, R. C. Nuclear control of respiratory chain expression in  
936 mammalian cells. *J Bioenerg Biomembr* **29**, 109-119,  
937 doi:10.1023/a:1022681828846 (1997).
- 938 26 Dang, C. V. *et al.* The c-Myc target gene network. *Semin Cancer Biol*  
939 **16**, 253-264, doi:10.1016/j.semcancer.2006.07.014 (2006).
- 940 27 Guo, Q. M. *et al.* Identification of c-myc responsive genes using rat  
941 cDNA microarray. *Cancer Res* **60**, 5922-5928 (2000).
- 942 28 In, T. S. H. *et al.* HEB is required for the specification of fetal IL-17-  
943 producing gammadelta T cells. *Nat Commun* **8**, 2004,  
944 doi:10.1038/s41467-017-02225-5 (2017).

- 945 29 Coffey, F. *et al.* The TCR ligand-inducible expression of CD73 marks  
946 gammadelta lineage commitment and a metastable intermediate in  
947 effector specification. *J Exp Med* **211**, 329-343,  
948 doi:10.1084/jem.20131540 (2014).
- 949 30 Turchinovich, G. & Hayday, A. C. Skint-1 identifies a common  
950 molecular mechanism for the development of interferon-gamma-  
951 secreting versus interleukin-17-secreting gammadelta T cells. *Immunity*  
952 **35**, 59-68, doi:10.1016/j.immuni.2011.04.018 (2011).
- 953 31 Lu, Y., Cao, X., Zhang, X. & Kovalovsky, D. PLZF Controls the  
954 Development of Fetal-Derived IL-17+Vgamma6+ gammadelta T Cells.  
955 *J Immunol* **195**, 4273-4281, doi:10.4049/jimmunol.1500939 (2015).
- 956 32 Tan, L. *et al.* Single-Cell Transcriptomics Identifies the Adaptation of  
957 Scart1(+) Vgamma6(+) T Cells to Skin Residency as Activated Effector  
958 Cells. *Cell Rep* **27**, 3657-3671 e3654, doi:10.1016/j.celrep.2019.05.064  
959 (2019).
- 960 33 McCully, M. L. *et al.* Skin Metabolites Define a New Paradigm in the  
961 Localization of Skin Tropic Memory T Cells. *J Immunol* **195**, 96-104,  
962 doi:10.4049/jimmunol.1402961 (2015).
- 963 34 Bartz, R. *et al.* Lipidomics reveals that adiposomes store ether lipids  
964 and mediate phospholipid traffic. *J Lipid Res* **48**, 837-847,  
965 doi:10.1194/jlr.M600413-JLR200 (2007).
- 966 35 Le Goffe, C., Vallette, G., Jarry, A., Bou-Hanna, C. & Laboissee, C. L.  
967 The in vitro manipulation of carbohydrate metabolism: a new strategy  
968 for deciphering the cellular defence mechanisms against nitric oxide  
969 attack. *Biochem J* **344 Pt 3**, 643-648, doi:10.1042/0264-6021:3440643  
970 (1999).
- 971 36 Bustamante, E. & Pedersen, P. L. High aerobic glycolysis of rat  
972 hepatoma cells in culture: role of mitochondrial hexokinase. *Proc Natl*  
973 *Acad Sci U S A* **74**, 3735-3739, doi:10.1073/pnas.74.9.3735 (1977).

- 974 37 Buck, M. D., O'Sullivan, D. & Pearce, E. L. T cell metabolism drives  
975 immunity. *J Exp Med* **212**, 1345-1360, doi:10.1084/jem.20151159  
976 (2015).
- 977 38 Menk, A. V. *et al.* Early TCR Signaling Induces Rapid Aerobic  
978 Glycolysis Enabling Distinct Acute T Cell Effector Functions. *Cell Rep*  
979 **22**, 1509-1521, doi:10.1016/j.celrep.2018.01.040 (2018).
- 980 39 Shin, B. *et al.* Mitochondrial Oxidative Phosphorylation Regulates the  
981 Fate Decision between Pathogenic Th17 and Regulatory T Cells. *Cell*  
982 *Rep* **30**, 1898-1909 e1894, doi:10.1016/j.celrep.2020.01.022 (2020).
- 983 40 Di Luccia, B., Gilfillan, S., Cella, M., Colonna, M. & Huang, S. C. ILC3s  
984 integrate glycolysis and mitochondrial production of reactive oxygen  
985 species to fulfill activation demands. *J Exp Med* **216**, 2231-2241,  
986 doi:10.1084/jem.20180549 (2019).
- 987 41 Schmolka, N. *et al.* Epigenetic and transcriptional signatures of stable  
988 versus plastic differentiation of proinflammatory gammadelta T cell  
989 subsets. *Nat Immunol* **14**, 1093-1100, doi:10.1038/ni.2702 (2013).
- 990 42 Schmolka, N., Wencker, M., Hayday, A. C. & Silva-Santos, B.  
991 Epigenetic and transcriptional regulation of gammadelta T cell  
992 differentiation: Programming cells for responses in time and space.  
993 *Semin Immunol* **27**, 19-25, doi:10.1016/j.smim.2015.01.001 (2015).
- 994 43 Gentles, A. J. *et al.* The prognostic landscape of genes and infiltrating  
995 immune cells across human cancers. *Nat Med* **21**, 938-945,  
996 doi:10.1038/nm.3909 (2015).
- 997 44 Legut, M., Cole, D. K. & Sewell, A. K. The promise of gammadelta T  
998 cells and the gammadelta T cell receptor for cancer immunotherapy.  
999 *Cell Mol Immunol* **12**, 656-668, doi:10.1038/cmi.2015.28 (2015).
- 1000 45 Baenke, F., Peck, B., Miess, H. & Schulze, A. Hooked on fat: the role  
1001 of lipid synthesis in cancer metabolism and tumour development. *Dis*  
1002 *Model Mech* **6**, 1353-1363, doi:10.1242/dmm.011338 (2013).

- 1003 46 Ma, X. *et al.* Cholesterol Induces CD8(+) T Cell Exhaustion in the  
1004 Tumor Microenvironment. *Cell Metab* **30**, 143-156 e145,  
1005 doi:10.1016/j.cmet.2019.04.002 (2019).
- 1006 47 Nakamizo, S. *et al.* High fat diet exacerbates murine psoriatic  
1007 dermatitis by increasing the number of IL-17-producing gammadelta T  
1008 cells. *Sci Rep* **7**, 14076, doi:10.1038/s41598-017-14292-1 (2017).
- 1009 48 Goldberg, E. L. *et al.* Ketogenic diet activates protective gammadelta T  
1010 cell responses against influenza virus infection. *Sci Immunol* **4**,  
1011 doi:10.1126/sciimmunol.aav2026 (2019).
- 1012 49 Michelet, X. *et al.* Metabolic reprogramming of natural killer cells in  
1013 obesity limits antitumor responses. *Nat Immunol* **19**, 1330-1340,  
1014 doi:10.1038/s41590-018-0251-7 (2018).
- 1015 50 Fischer, K. *et al.* Inhibitory effect of tumor cell-derived lactic acid on  
1016 human T cells. *Blood* **109**, 3812-3819, doi:10.1182/blood-2006-07-  
1017 035972 (2007).
- 1018 51 Wang, Z. *et al.* Glycolysis and Oxidative Phosphorylation Play Critical  
1019 Roles in Natural Killer Cell Receptor-Mediated Natural Killer Cell  
1020 Functions. *Front Immunol* **11**, 202, doi:10.3389/fimmu.2020.00202  
1021 (2020).
- 1022 52 Almeida, A. R. *et al.* Delta One T Cells for Immunotherapy of Chronic  
1023 Lymphocytic Leukemia: Clinical-Grade Expansion/Differentiation and  
1024 Preclinical Proof of Concept. *Clin Cancer Res* **22**, 5795-5804,  
1025 doi:10.1158/1078-0432.CCR-16-0597 (2016).
- 1026 53 Di Lorenzo, B. *et al.* Broad Cytotoxic Targeting of Acute Myeloid  
1027 Leukemia by Polyclonal Delta One T Cells. *Cancer Immunol Res* **7**,  
1028 552-558, doi:10.1158/2326-6066.CIR-18-0647 (2019).
- 1029 54 Correia, D. V. *et al.* Differentiation of human peripheral blood Vdelta1+  
1030 T cells expressing the natural cytotoxicity receptor NKp30 for  
1031 recognition of lymphoid leukemia cells. *Blood* **118**, 992-1001,  
1032 doi:10.1182/blood-2011-02-339135 (2011).
- 1033

1034

1035

1036 **Figure Legends**

1037 **Figure 1. Intra-tumoural  $\gamma\delta$  T cell subsets display distinct metabolic**  
1038 **profiles.**

1039 **(a)** Experimental design: E0771 breast or MC38 colon cancer cell lines were  
1040 injected in WT mice; 6 and 15 days later, tumours were extracted for  
1041 metabolic analysis of  $\gamma\delta$  T cells using SCENITH™. Inhibitors for different  
1042 metabolic pathways were added for 30min followed by an incubation of 15min  
1043 with puromycin. Mean fluorescence intensity (MFI) of puromycin is analyzed  
1044 by flow cytometry in  $\gamma\delta^{17}$  and  $\gamma\delta^{\text{IFN}}$  subpopulations for each condition. **(b-e)**  
1045 Puromycin MFI of  $\gamma\delta^{17}$  and  $\gamma\delta^{\text{IFN}}$  T cells from E0771 **(b,d)** and MC38 **(c,e)**  
1046 tumour-bearing mice in control conditions (Co) or after the addition of 2-  
1047 deoxy-D-glucose (DG), oligomycin (O) or both inhibitors (DGO). Graph shows  
1048 the percentage of glucose dependence, mitochondrial dependence, glycolytic  
1049 capacity and fatty acid and amino acid oxidation (FaaO) capacity of tumour-  
1050 infiltrating  $\gamma\delta^{17}$  and  $\gamma\delta^{\text{IFN}}$  cells isolated either 6 **(d,e)** or 15 **(b,c)** days after  
1051 cancer cell line injection. Data are representative of two independent  
1052 experiments (n=5 mice per group in each experiment). pi: post-injection.  
1053  $\gamma\delta^{17}$  and  $\gamma\delta^{\text{IFN}}$  T cells represents IL-17 and IFN- $\gamma$ -producing  $\gamma\delta$  T cells,  
1054 respectively. Error bars show mean  $\pm$  SEM, \*p < 0.05; \*\*p < 0.01; \*\*\*\*<0.0001  
1055 using unpaired Student's t-test.

1056

1057 **Figure 2: Peripheral  $\gamma\delta$  T cell subsets show different mitochondrial and**  
1058 **metabolic phenotypes.**

1059 **(a)** Representative plots (left) and summary graphs (right) of the MFI of  
1060 mitotracker and tetramethylrhodamine methyl ester (TMRM) in  $\gamma\delta^{27-}$  ( $\gamma\delta^{17}$ ) and  
1061  $\gamma\delta^{27+}$  ( $\gamma\delta^{\text{IFN}}$ ) T cells *ex vivo* from LNs of C57BL/6 mice (n=7; data pooled from  
1062 2 experiments). **(b)** Representative confocal images (left) of  $\gamma\delta^{17}$  and  $\gamma\delta^{\text{IFN}}$  T  
1063 cells stained with mitotracker (green) and Hoechst 33342 (blue). Scale bar  
1064 represents 5 $\mu$ M. Analysis of mitotracker staining relative to cell size (right) in  
1065  $\gamma\delta^{17}$  and  $\gamma\delta^{\text{IFN}}$  cells *ex vivo*. Relative mitotracker was calculated by dividing the  
1066 MFI of mitotracker by the MFI of FSC-A and multiplying by 100 (n=7, data

1067 pooled from 2 independent experiments). **(c)** Tetramethylrhodamine ethyl  
1068 ester (TMRE) MFI of  $\gamma\delta^{17}$  and  $\gamma\delta^{\text{IFN}}$  T cells from skin draining LNs, mesenteric  
1069 LNs, spleen and liver of WT mice. Data are representative of 3 independent  
1070 experiments (n=3 mice per group and experiment). **(d)** Seahorse analysis of  
1071 extracellular acidification rate (ECAR) and oxygen consumption rate (OCR) of  
1072  $\gamma\delta^{17}$  and  $\gamma\delta^{\text{IFN}}$  T cells (expanded *in vitro*) from LNs ( $\gamma\delta^{17}$  n=2,  $\gamma\delta^{\text{IFN}}$  n=5, data  
1073 representative of 3 independent experiments). **(e)** Energy map showing ECAR  
1074 vs OCR of  $\gamma\delta^{17}$  and  $\gamma\delta^{\text{IFN}}$  T cells. Each symbol represents average basal  
1075 metabolism. **(f)** Basal glycolytic rate, glycolytic capacity and basal OxPhos of  
1076  $\gamma\delta^{17}$  (n=3) and  $\gamma\delta^{\text{IFN}}$  (n=8) cell subsets (data pooled from 2 independent  
1077 experiments). **(g)** Percentage of glucose dependence, mitochondrial  
1078 dependence, glycolytic capacity and fatty acid and amino acid oxidation  
1079 (FaaO) capacity of  $\gamma\delta^{17}$  and  $\gamma\delta^{\text{IFN}}$  cells from spleen and draining lymph nodes  
1080 (dLNs). Data are representative of three independent experiments (n=5 mice  
1081 per group and per experiment). **(h,i)** OxPhos-related genes (*Ndufa11*,  
1082 *Ndufa13*, *Sdha*, *Cox6a1*, *Cox7a1*, *Cox15*, *Nrf1*) and glycolysis-related genes  
1083 (*Pgm1*, *Pgm2*, *Gpi1*, *Pgam1*, *Myc*) were measured by qPCR in purified  $\gamma\delta^{17}$   
1084 (n=4) and  $\gamma\delta^{\text{IFN}}$  (n=4) T cells from spleen and dLN from WT mice. **(j)**  
1085 Representative plot (left) and percentages (right) of Myc-GFP+  $\gamma\delta^{17}$  and  $\gamma\delta^{\text{IFN}}$   
1086 T cells from LNs of Myc-GFP reporter mice (n=2). Error bars show  
1087 mean  $\pm$  SEM or SD, \*p < 0.05; \*\*p < 0.01; \*\*\*p < 0.001, \*\*\*\*p < 0.0001 using  
1088 unpaired Student's t-test.

1089

1090 **Figure 3:  $\gamma\delta$  T cell subsets are metabolically programmed in the thymus.**

1091 **(a)** Puromycin MFI of  $\gamma\delta^{17}$  (CD44<sup>hi</sup>CD45RB<sup>-</sup>) and  $\gamma\delta^{\text{IFN}}$  (CD44<sup>+</sup>CD45RB<sup>+</sup>) T  
1092 cells from WT adult thymus in resting conditions (Co) and after the addition of  
1093 2-deoxy-D-glucose (DG), oligomycin (O) or both (DGO). Histogram (right)  
1094 shows the percentage of glucose dependency (white), mitochondrial  
1095 dependency (blue), glycolytic capacity (red) and fatty acid and amino acid  
1096 oxidation (FaaO) capacity (purple) of thymic  $\gamma\delta^{17}$  and  $\gamma\delta^{\text{IFN}}$  cells. Data are  
1097 representative of two independent experiments (n=5 mice per group and per  
1098 experiment). **(b)** Histograms shows the percentage of glucose dependency

1099 (white), mitochondrial dependency (blue), glycolytic capacity (red) and fatty  
1100 acid and amino acid oxidation (FaaO) capacity (purple) of  $\gamma\delta^{17}$  and  $\gamma\delta^{\text{IFN}}$  T  
1101 cells from WT newborn thymus (d3). Data are representative of three  
1102 independent experiments (n=6 mice per group and per experiment). **(c)** Flow  
1103 cytometry profile and Tetramethylrhodamine ethyl ester (TMRE) MFI of thymic  
1104  $\gamma\delta^{24+}$  precursors treated or not with FCCP. Data are representative of 3  
1105 independent experiments (data points represent at least 4 lobes pooled per  
1106 group and per experiment). **(d)** Flow cytometry profiles and TMRE MFI of  
1107 thymic  $\gamma\delta^{\text{TN}}$  (CD44<sup>-</sup>CD45RB<sup>-</sup>),  $\gamma\delta^{17}$  (CD44<sup>hi</sup>CD45RB<sup>-</sup>) and  $\gamma\delta^{\text{IFN}}$   
1108 (CD44<sup>+</sup>CD45RB<sup>+</sup>) cells treated or not with FCCP. Data are representative of 3  
1109 independent experiments (data points represent at least 4 lobes pooled per  
1110 group and per experiment). **(e)** Imagestream analysis of  $\gamma\delta^{17}$  and  $\gamma\delta^{\text{IFN}}$  cells  
1111 stained with either mitotracker green or TMRE. Data are representative of 2  
1112 independent experiments. **(f)** O<sub>2</sub> consumption rates (OCR) of  $\gamma\delta^{17}$  and  $\gamma\delta^{\text{IFN}}$   
1113 cells were measured by Seahorse analysis in real-time under basal conditions  
1114 and in response to indicated mitochondrial inhibitors. **(g)** Histograms show  
1115 maximal respiration potential and spare respiratory capacity by measuring  
1116 oxygen consumption rates (OCR) of  $\gamma\delta^{17}$  and  $\gamma\delta^{\text{IFN}}$  cells from thymuses of 5-  
1117 day old B6 pups. Data are representative of 3 independent experiments  
1118 (pooled thymic lobes from n>10 mice per group per experiment). **(h-j)** Flow  
1119 cytometry profiles of thymic  $\gamma\delta^{\text{TN}}$ ,  $\gamma\delta^{17}$  and  $\gamma\delta^{\text{IFN}}$  cells from 7-day FTOC of E15  
1120 thymic lobes either with media containing low (5mM) or high (25mM) glucose  
1121 **(h)**, or with or without 2-deoxy-d-glucose (2-DG) **(i)** or metformin **(j)**.  
1122 Histograms show the number of  $\gamma\delta^{17}$  cells and  $\gamma\delta^{17}/\gamma\delta^{\text{IFN}}$  cell ratio. Data are  
1123 representative of 2 **(h)** or 3 **(i-j)** independent experiments (at least 4 lobes  
1124 pooled per group per experiment). Error bars show mean  $\pm$  SEM or SD,  
1125 \*p < 0.05, \*\*p < 0.01, \*\*\*p < 0.001, \*\*\*\*p < 0.0001 using unpaired Student's t-  
1126 test.

1127

1128 **Figure 4: Distinct mitochondrial activities underlie effector fate of thymic**  
1129  **$\gamma\delta$  T cell progenitors.**



1130 **(a,b)** Flow cytometry profiles and percentage of thymic  $\gamma\delta^{17}$  and  $\gamma\delta^{\text{IFN}}$  cell  
1131 output from post-sorted  $\text{TMRE}^{\text{lo}}$  and  $\text{TMRE}^{\text{hi}}$   $\gamma\delta^{\text{TN}}$  cells **(a)** or  $\gamma\delta^{24+}$  cells **(b)**  
1132 after 5-day culture on OP9DL1 cells. Data are representative of 3 independent  
1133 experiments (n = 4 mice pooled per group per experiment). **(c)** Percentage of  
1134  $V\gamma 1^+$  and  $V\gamma 4^+$  cells in  $\text{TMRE}^{\text{lo}}$  and  $\text{TMRE}^{\text{hi}}$   $\gamma\delta^{24+}$  and  $\gamma\delta^{24-}$  subsets. Data are  
1135 representative of 3 independent experiments (cells sorted from n=4 mice  
1136 pooled per group per experiment). **(d)** TMRE MFI of thymic  $\gamma\delta^{\text{TN}}$  ( $\text{CD44}^-$   
1137  $\text{CD45RB}^-$ ),  $\text{CD24}^- \text{CD44}^- \text{CD45RB}^+$   $\gamma\delta$  T cells and  $\gamma\delta^{\text{IFN}}$  cells ( $\text{CD44}^+ \text{CD45RB}^+$ )  
1138 from 6-day FTOC of E17 B6 thymic lobes. **(e)** TMRE staining in  $\text{CD24}^- \text{CD73}^+$ ,  
1139  $\text{CD24}^- \text{CD73}^-$ ,  $\text{CD24}^+ \text{CD73}^+$  and  $\text{CD24}^+ \text{CD73}^-$   $\gamma\delta$  T cells from 7-day FTOC of  
1140 E15 B6 thymic lobes. **(f)** TMRE staining in  $\text{CD25}^- \text{CD24}^+$  ( $\gamma\delta^{24+}$  cells),  $\text{CD25}^{\text{med}}$ ,  
1141  $\text{CD25}^{\text{hi}}$  and  $V\gamma 5^+$   $\gamma\delta$  progenitors from E15 thymus. **(g)** Flow cytometry profiles  
1142 of thymic  $\gamma\delta^{\text{TN}}$ ,  $\gamma\delta^{17}$  and  $\gamma\delta^{\text{IFN}}$  cells from 6-day FTOC of E17 B6 thymic lobes  
1143 stimulated or not with anti-TCR $\delta$  mAb (GL3; 1 $\mu\text{g}/\text{ml}$ ). Graph shows  
1144 percentage of  $\gamma\delta^{17}$  and  $\gamma\delta^{\text{IFN}}$  cells in each condition. **(h)** FACS-sorted  
1145  $\gamma\delta^{24+} \text{TMRE}^{\text{hi}}$  cells from E17 thymi were cultured (or not) for 5h with different  
1146 concentrations (as indicated) of anti-TCR $\delta$  mAb (GL3). TMRE levels were  
1147 analysed by flow cytometry in  $\gamma\delta^{24-}$  and  $\gamma\delta^{24+}$  cells. Data are representative of  
1148 3 independent experiments (n=4 mice pooled per group per experiment). **(i)**  
1149 Experimental design for single-cell RNAseq (10x Genomics) on  $\text{TMRE}^{\text{lo}}$  and  
1150  $\text{TMRE}^{\text{hi}}$   $\gamma\delta^{24+}$  cells from E15 + 2d FTOC. **(j)** Clustering of single  $\text{TMRE}^{\text{lo}}$  and  
1151  $\text{TMRE}^{\text{hi}}$   $\gamma\delta^{24+}$  cells using UMAP. **(k)** GO term analysis of genes upregulated in  
1152  $\text{TMRE}^{\text{lo}}$  versus  $\text{TMRE}^{\text{hi}}$   $\gamma\delta^{24+}$  cells. **(l)** Heatmap of differentially upregulated  
1153 genes from comparison of  $\text{TMRE}^{\text{lo}}$  and  $\text{TMRE}^{\text{hi}}$   $\gamma\delta^{24+}$  cells. Genes are grouped  
1154 in relation to their function in either OxPhos or glucose metabolism. Error bars  
1155 show mean  $\pm$  SD, \*p < 0.05, \*\*p < 0.01, \*\*\*p < 0.001, \*\*\*\*p < 0.0001 using  
1156 unpaired Student's t-test.

1157

1158 **Figure 5.  $\gamma\delta^{17}$  cells show higher lipid uptake and lipid droplet content**  
1159 **than  $\gamma\delta^{\text{IFN}}$  cells.**

1160 **(a)** Experimental set up for bulk RNA-sequencing of PLZF<sup>+</sup> ( $\gamma\delta^{17}$ ) and PLZF<sup>-</sup>  
1161 ( $\gamma\delta^{\text{IFN}}$ ) cells isolated from PLZF-GFP (*Zbtb16*<sup>GFP</sup>) mice. **(b)** Quadrant plot of  
1162 genes upregulated in tissue resident PLZF<sup>+</sup>  $\gamma\delta$  T cells (lower right), lymphoid  
1163 PLZF<sup>+</sup>  $\gamma\delta$  T cells (upper left), PLZF<sup>+</sup>  $\gamma\delta$  T cells from all tissues (upper right) or  
1164 PLZF<sup>-</sup>  $\gamma\delta$  T cells from all tissues (lower left). **(c)** Representative histogram of  
1165 neutral lipid staining (LipidTOX) in *ex vivo*  $\gamma\delta^{17}$  (CD27<sup>-</sup>) and  $\gamma\delta^{\text{IFN}}$  (CD27<sup>+</sup>) cells  
1166 from LNs. **(d)** LipidTOX MFI in  $\gamma\delta^{17}$  and  $\gamma\delta^{\text{IFN}}$  cells *ex vivo* from LNs as shown  
1167 in (a) (n=11, data pooled from 3 independent experiments). **(e)** LipidTOX MFI  
1168 in  $\gamma\delta^{17}$  and  $\gamma\delta^{\text{IFN}}$  cells from spleen, LNs, lungs, adipose, liver and skin (n=5-8,  
1169 data pooled from 2 independent experiments). **(f)** Confocal imaging of  $\gamma\delta^{17}$   
1170 and  $\gamma\delta^{\text{IFN}}$  cells expanded *in vitro* and stained with LipidTOX (red) and Hoechst  
1171 33342 (blue). Scale bar represents 5 $\mu$ M (data representative of a minimum 10  
1172 images from 2 independent experiments). **(g)** Quantification of confocal  
1173 imaging as shown in (d) (each data point represents the average per cell per  
1174 image). **(h)** Quantification of triglyceride (TAG) levels from  $\gamma\delta^{17}$  and  $\gamma\delta^{\text{IFN}}$  cells  
1175 expanded *in vitro* (n=7, each symbol represents one biological replicate). **(i)**  
1176 Filipin III staining of  $\gamma\delta^{17}$  and  $\gamma\delta^{\text{IFN}}$  cells *ex vivo* from LNs. Representative  
1177 histogram (left) and MFI (right) (n=6, data pooled from 2 independent  
1178 experiments). **(j)** Representative histogram of Bodipy-FL-C<sub>16</sub> uptake in  $\gamma\delta^{17}$   
1179 and  $\gamma\delta^{\text{IFN}}$  cells from LNs *ex vivo* (n=8, data pooled from 2 independent  
1180 experiment). **(k)** Representative plots of Bodipy-FL-C<sub>16</sub> uptake and IL-17 or  
1181 IFN- $\gamma$  production by  $\gamma\delta^{17}$  and  $\gamma\delta^{\text{IFN}}$  cells from LNs stimulated with  
1182 PMA/ionomycin. **(l)** Bodipy-FL-C<sub>16</sub> MFI in IFN- $\gamma$ <sup>+</sup> and IL-17<sup>+</sup>  $\gamma\delta$  T cells (n=4,  
1183 data representative of 3 independent experiments). **(m)** Representative plot of  
1184 V $\gamma$ 1 and V $\gamma$ 4 expression in total  $\gamma\delta$  T cells and percentage Bodipy-FL-C<sub>16</sub>  
1185 uptake by LN  $\gamma\delta$  T cell subsets (V $\gamma$ 1<sup>+</sup>, V $\gamma$ 4<sup>+</sup>, V $\gamma$ 1<sup>-</sup>4<sup>-</sup>) (n=6, data pooled from 2  
1186 independent experiment). **(n)** Representative IFN- $\gamma$  and IL-17 production by  
1187 V $\gamma$ 4<sup>+</sup>  $\gamma\delta$  T cells from LNs and percentage Bodipy-FL-C<sub>16</sub> uptake by V $\gamma$ 4<sup>+</sup>IFN- $\gamma$ <sup>+</sup>  
1188 and V $\gamma$ 4<sup>+</sup>IL-17<sup>+</sup>  $\gamma\delta$  cells (n=6, data pooled from 2 independent experiments).  
1189 **(o)** Percentage Bodipy CholEsteryl FL-C<sub>12</sub> uptake by  $\gamma\delta^{17}$  (CD27<sup>-</sup>) and  $\gamma\delta^{\text{IFN}}$   
1190 (CD27<sup>+</sup>) cells from LNs *ex vivo* (n=6, data pooled from 2 independent

1191 experiments). Error bars show mean  $\pm$  SD, \* $p < 0.05$ , \*\* $p < 0.01$ , \*\*\* $p < 0.001$ ,  
1192 \*\*\*\* $p < 0.0001$  using unpaired Student's t-test.

1193

1194

1195

1196 **Figure 6. High fat diet promotes the expansion of  $\gamma\delta^{17}$  cells in lymph**  
1197 **nodes and within tumours.**

1198 **(a)** Respiratory exchange ratio (RER) of mice fed SFD or HFD for 8 weeks  
1199 (n=3, data from 1 experiment). **(b)** Bar graphs showing the percentage and  
1200 absolute numbers of CD3<sup>+</sup>  $\gamma\delta$  T cells from LNs of standard fat diet (SFD) and  
1201 high fat diet (HFD) mice (n=9, data pooled from 3 independent experiments).  
1202 **(c)** Proportion of  $\gamma\delta^{17}$  (CD27<sup>-</sup>) and  $\gamma\delta^{\text{IFN}}$  (CD27<sup>+</sup>) T cells in LNs of SFD and  
1203 HFD fed mice (n=9, data pooled from 3 independent experiments). **(d)**  
1204 Percentage and absolute numbers of CD27<sup>+</sup> IFN- $\gamma$ <sup>+</sup> and CD27<sup>-</sup> IL-17<sup>+</sup>  $\gamma\delta$  T  
1205 cells from LNs of SFD and HFD mice (n=9, data pooled from 3 independent  
1206 experiments). **(e)** Proportion of infiltrating  $\gamma\delta^{17}$  cells in spleen, draining LN and  
1207 tumour in the B16 tumour model (dLN and tumour n=30, data pooled from 4  
1208 independent experiments, spleen n=7, naïve LN n=5). **(f)** Bar graph showing  
1209 the percentage of  $\gamma\delta^{17}$  and  $\gamma\delta^{\text{IFN}}$  cells infiltrating tumours (n=9, data pooled  
1210 from 2 experiments). **(g)** Bar graph represents the size of tumours (mm<sup>3</sup>) in  
1211 SFD and HFD fed mice. **(h)** Bar graph showing proportion of infiltrating  $\gamma\delta^{17}$   
1212 (CD27<sup>-</sup>) and  $\gamma\delta^{\text{IFN}}$  (CD27<sup>+</sup>) cells in tumours of SFD and HFD fed mice (SFD  
1213 n=10, HFD n=12, data pooled from 2 independent experiments). **(i)**  
1214 Representative plots of IL-17 and IFN- $\gamma$  expression in  $\gamma\delta$  T cells infiltrating  
1215 tumours of SFD and HFD fed mice. Bar graphs represent the percentage of  
1216  $\gamma\delta^{17}$  and  $\gamma\delta^{\text{IFN}}$  cells infiltrating tumours (SFD n=17, HFD n=20, data pooled  
1217 from 3 independent experiments). **(j)** Bar graph showing the number/mm<sup>3</sup> of  
1218  $\gamma\delta^{17}$  and  $\gamma\delta^{\text{IFN}}$  cells in tumours of mice on SFD or HFD (SFD n=7, HFD n=8,  
1219 data pooled from 2 independent experiments). **(k)** Plots of proliferating Ki67<sup>+</sup>  
1220  $\gamma\delta^{17}$  cells cultured for 5h with or without cholesterol-loaded cyclodextrin (CLC).  
1221 Graph represents the percentage of Ki67<sup>+</sup>  $\gamma\delta^{17}$  cells (data are representative

1222 of two independent experiments; pool of 3-5 mice per experiment). **(l)**  $\gamma\delta^{17}$   
1223 cells cultured (or not) with cholesterol-loaded cyclodextrin (CLC) for 5h were  
1224 injected s.c. into E0771 tumours at d7 and d9 after tumour cell injection.  
1225 Representative picture of tumours observed at day 11 post-E0771 cell  
1226 inoculation. **(m)** Graph showing tumour weight at day 11 post-E0771  
1227 inoculation. **(n)** E0771 tumour growth was monitored every two days after  
1228 inoculation ((l-n) data are representative of three independent experiments  
1229 (pool of 2-5 mice per experiment). Error bars show mean  $\pm$  SD, \* $p < 0.05$ ,  
1230 \*\* $p < 0.01$ , \*\*\* $p < 0.001$ , \*\*\*\* $p < 0.0001$  using unpaired Student's t-test or  
1231 ANOVA test.

1232

1233 **Figure 7: Glucose supplementation enhances the effector functions of**  
1234  **$\gamma\delta^{\text{IFN}}$  cells.**

1235 **(a)** Glucose uptake assessed upon i.v. injection of fluorescent 2-NBDG in  
1236 tumour-bearing mice. Tumours were harvested 15 min later for analysis.  
1237 Histogram represents 2-NBDG uptake in  $\gamma\delta^{17}$  and  $\gamma\delta^{\text{IFN}}$  cells. **(b-i)** Purified  
1238 splenic and peripheral lymph nodes  $\gamma\delta^{\text{IFN}}$  T cells ( $\text{CD3}^+\text{TCR}\gamma\delta^+\text{CD27}^+$ ) were  
1239 cultured in the presence of IL-7 with media containing low glucose (5mM), 2-  
1240 deoxyglycose (2-DG), high glucose (50mM) or galactose (20mM) for 78h. **(b)**  
1241 Plots of peripheral  $\gamma\delta^{\text{IFN}}$  T cells cultured with IL-7 and media containing low  
1242 glucose, 2-DG or high glucose. Histogram represents the fold change in  
1243 number of  $\gamma\delta^{\text{IFN}}$  T cells cultured with 2-DG or high glucose versus low glucose.  
1244 **(c)** Fold change in number of proliferating Ki-67<sup>+</sup>  $\gamma\delta^{\text{IFN}}$  cells cultured with 2-DG  
1245 or high glucose versus low glucose. **(d,e)** IFN- $\gamma$  **(d)** and T-bet **(e)** expression  
1246 was analysed by flow cytometry in  $\gamma\delta^{\text{IFN}}$  cells incubated with media containing  
1247 low glucose, 2-DG or high glucose. Histograms show the MFI of IFN- $\gamma$  and T-  
1248 bet. **(f)** Flow cytometry profiles of peripheral  $\gamma\delta^{\text{IFN}}$  T cells cultured with IL-7 and  
1249 media containing glucose (50mM) or galactose (20mM). Histogram represents  
1250 the numbers of  $\gamma\delta^{\text{IFN}}$  T cells. **(g,h)** IFN- $\gamma$  **(g)** and T-bet **(h)** expression was  
1251 analysed by flow cytometry in  $\gamma\delta^{\text{IFN}}$  cells incubated with media containing  
1252 glucose or galactose. Histograms show the MFI of IFN- $\gamma$  and T-bet.  
1253 **(i)** Representative histograms and summary of killing assay *in vitro*

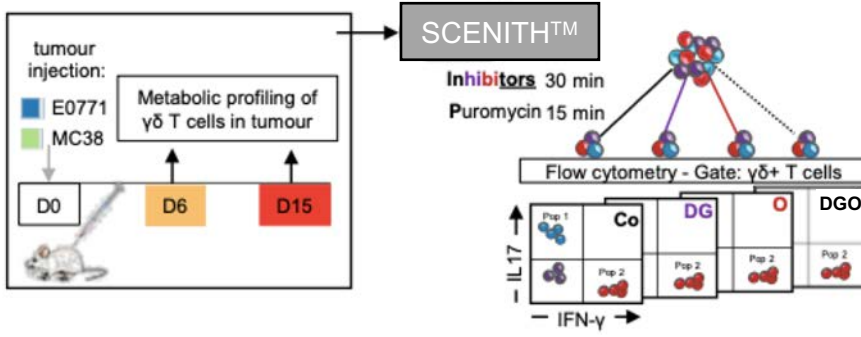
1254 of E0771 tumour cells by  $\gamma\delta^{\text{IFN}}$  T cells previously supplemented (or not) with  
1255 glucose (5h pre-incubation). **(j)** Representative picture of tumours observed at  
1256 day 11 post-E0771 inoculation.  $\gamma\delta^{\text{IFN}}$  cells supplemented (or not) with glucose  
1257 for 5h were injected into the tumour at d7 and d9 after tumour cell injection.  
1258 **(k)** The E0771 tumour growth was monitored every two days during 11 days  
1259 after E0771 inoculation (data are representative of two **(i-k)** or four **(b-h)**  
1260 independent experiments; n = 5-10 mice per group and per experiment). Error  
1261 bars show mean  $\pm$  SEM, \*p < 0.05, \*\*p < 0.01, \*\*\*p < 0.001, \*\*\*\*p < 0.0001  
1262 using unpaired Student's t-test or ANOVA test.

1263

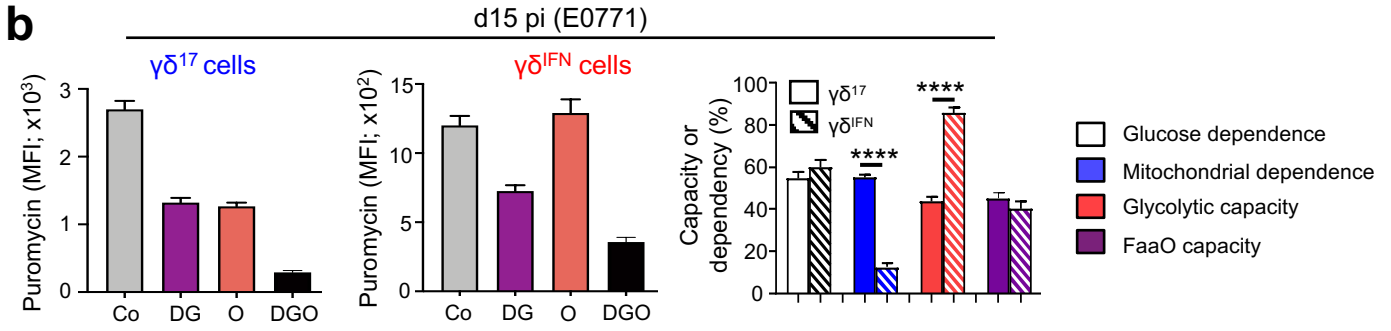
1264

# Figure 1

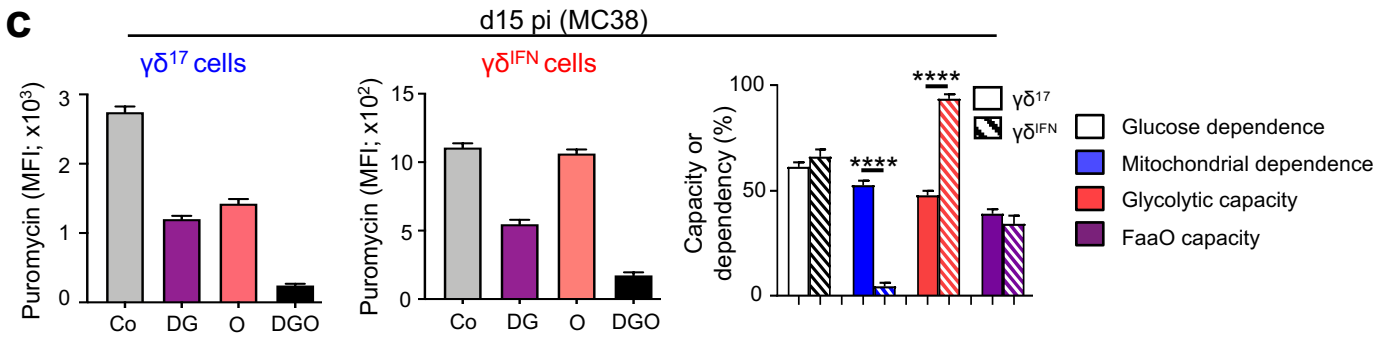
**a**



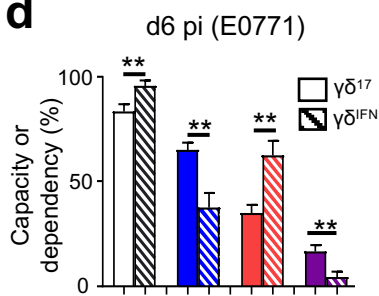
**b**



**c**



**d**



**e**

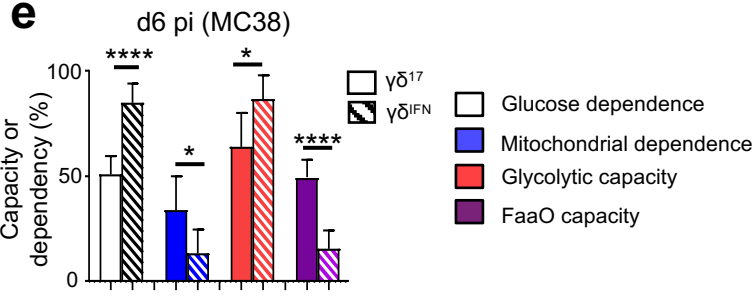


# Figure 2

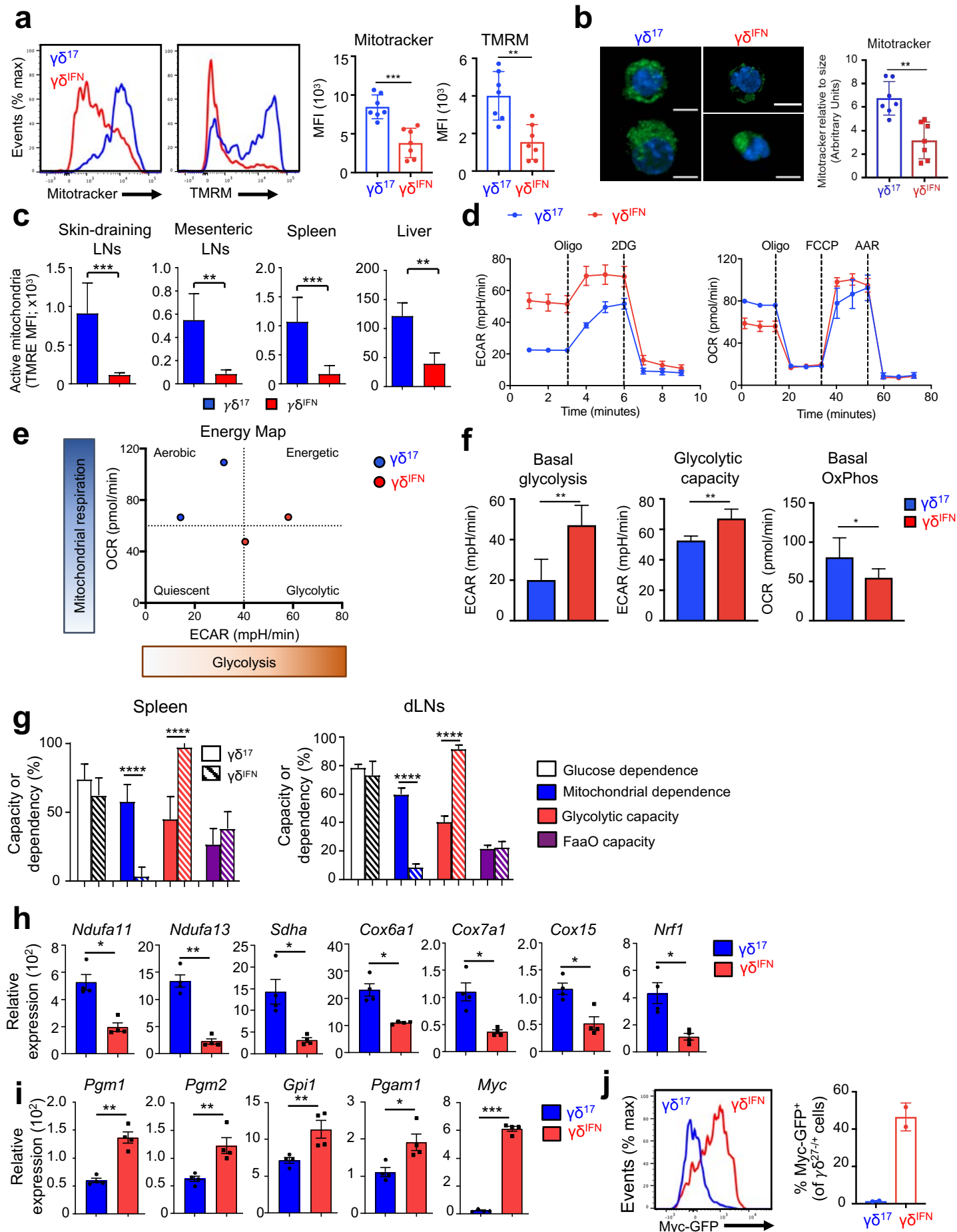
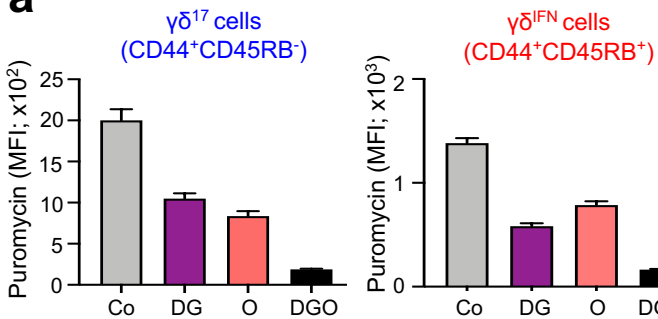
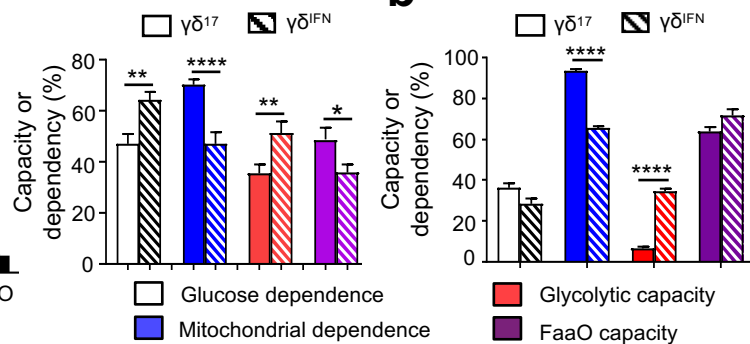


# Figure 3

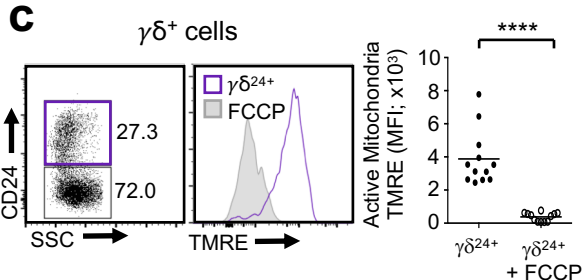
**a**



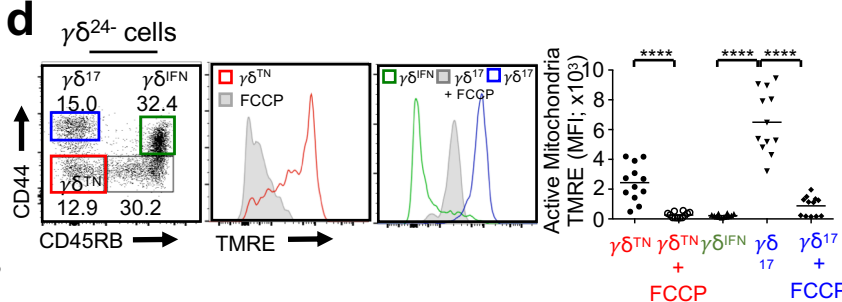
**b**



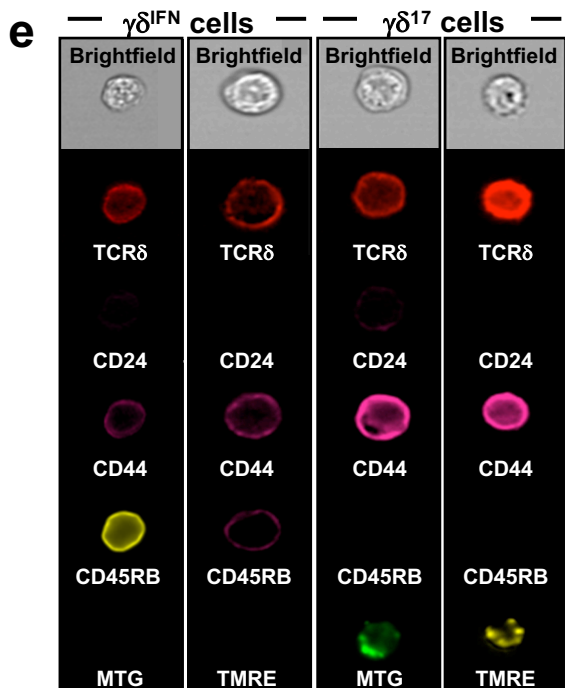
**c**



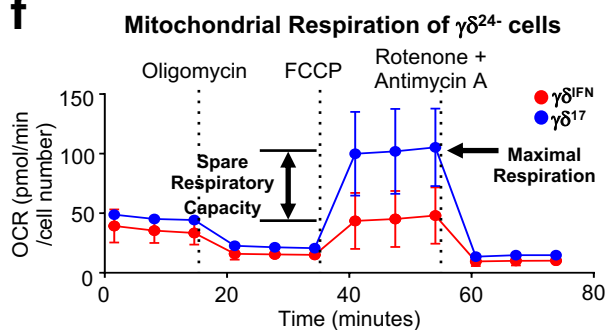
**d**



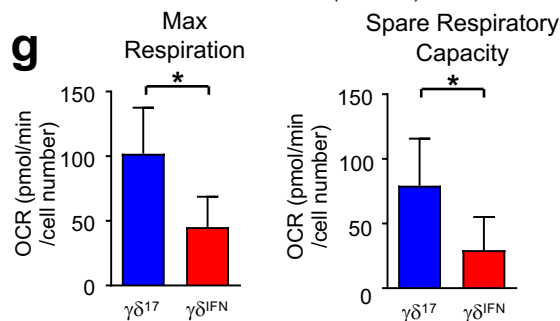
**e**



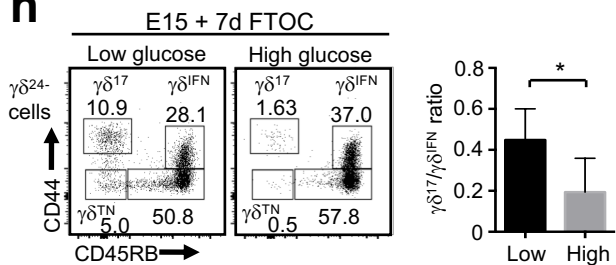
**f**



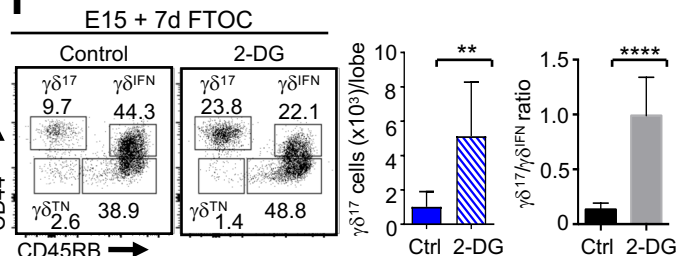
**g**



**h**



**i**



**j**

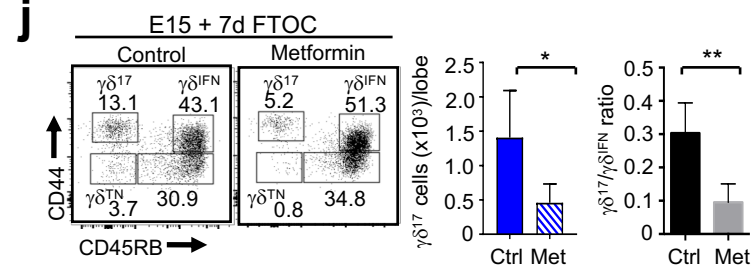




# Figure 4

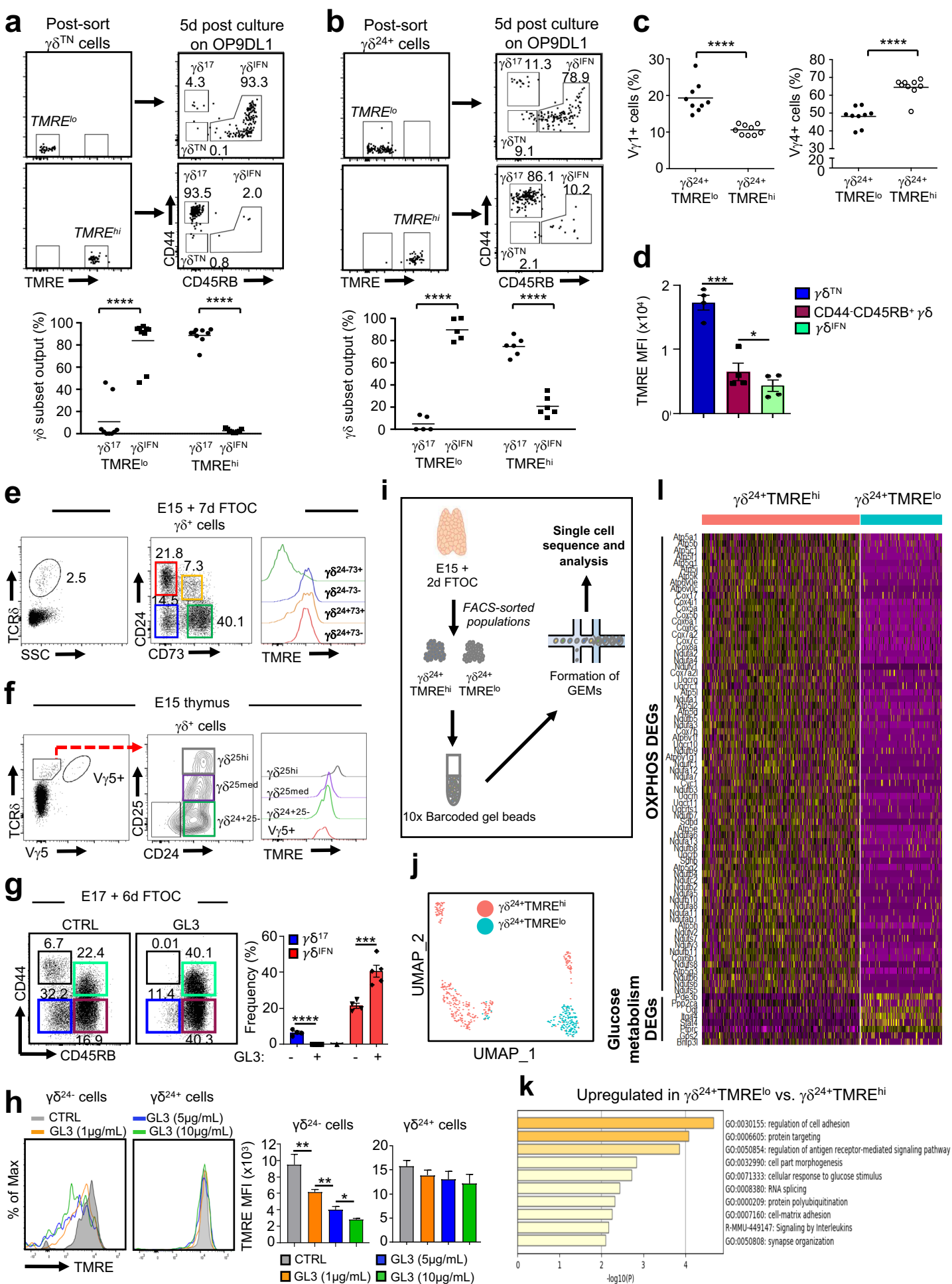


# Figure 5

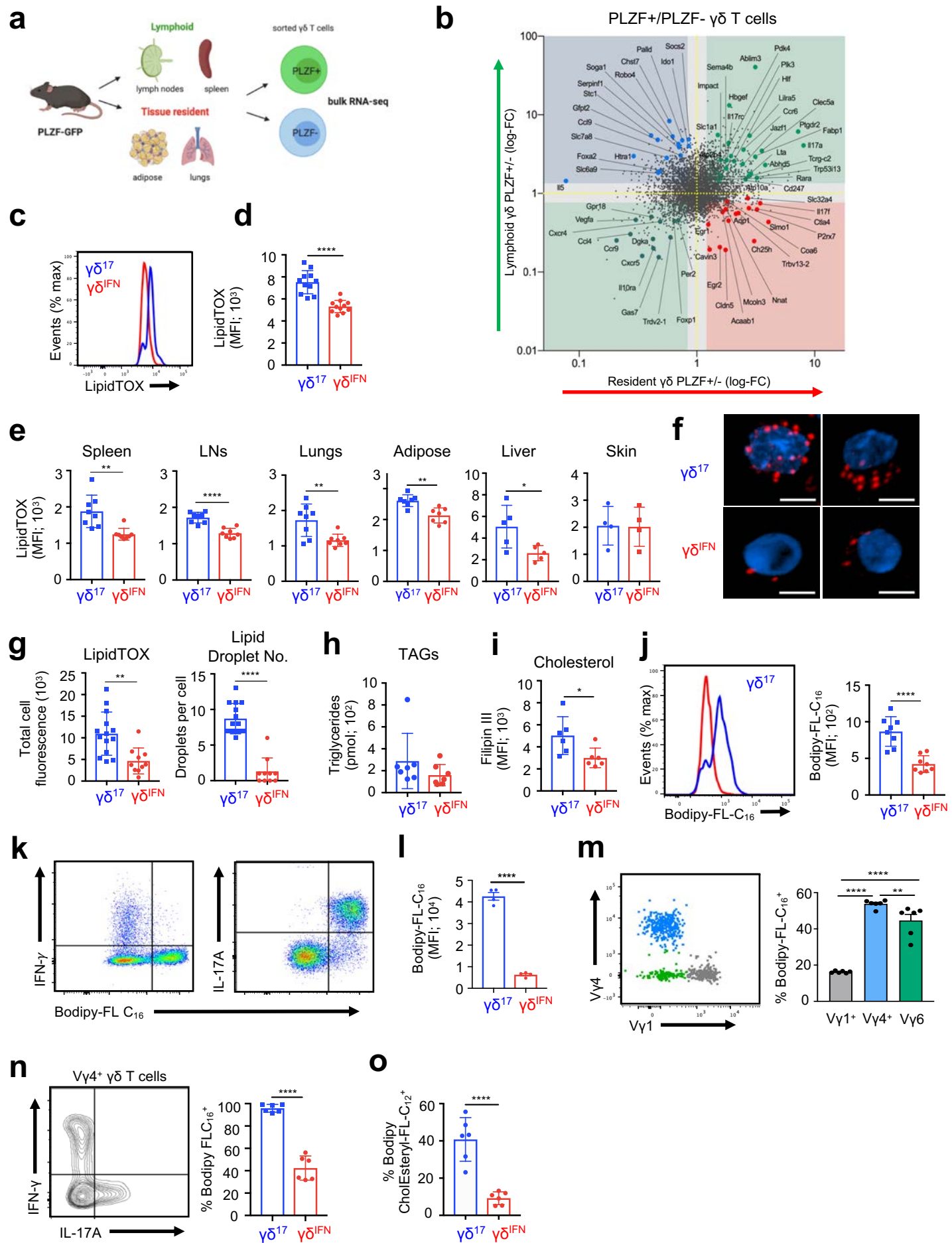


# Figure 6

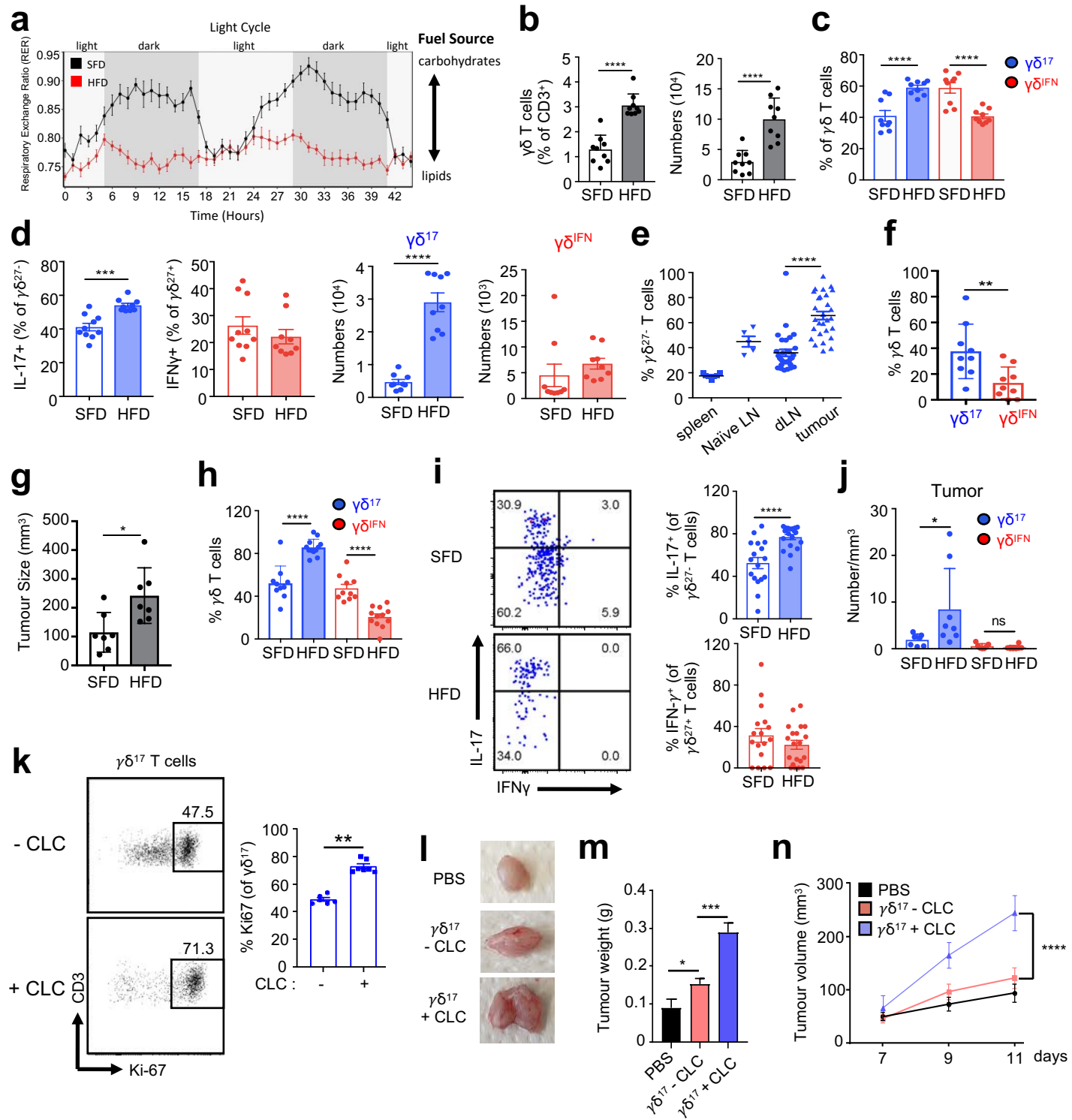


# Figure 7

